

# Modeling Grain Alignment by Radiative Torques and Hydrogen Formation Torques in Reflection Nebula

Thiem Hoang<sup>1\*2</sup>, A. Lazarian<sup>3</sup>, and B-G Andersson<sup>4</sup>

<sup>1</sup> Canadian Institute for Theoretical Astrophysics, University of Toronto, 60 St. George Street, Toronto, ON M5S 3H8, Canada,

<sup>2</sup> Institut für Theoretische Physik, Lehrstuhl IV: Weltraum- und Astrophysik, Ruhr-Universität Bochum, 44780 Bochum, Germany,

<sup>3</sup> Department of Astronomy, University of Wisconsin-Madison, Madison, WI 53705, USA,

<sup>4</sup> SOFIA Science Center, Universities Space Research Association, NASA Ames Research Center, M.S. N232-12 Moffett Field, CA 94035, USA

17 October 2019

## ABSTRACT

Reflection nebulae–dense cores–illuminated by surrounding stars offer a unique opportunity to directly test our quantitative model of grain alignment based on radiative torques (RATs) and to explore new effects arising from additional torques. In this paper, we first perform detailed modeling of grain alignment by RATs for the IC 63 reflection nebula illuminated both by a nearby  $\gamma$  Cas star and the diffuse interstellar radiation field. We calculate linear polarization  $p$  of background stars by radiatively aligned grains and explore the variation of fractional polarization ( $p/A_V$ ) with visual extinction  $A_V$  across the cloud. We show that the variation of  $p/A_V$  from the surface of the dayside toward the IC 63 center can be described by a power law  $p/A_V \propto A_V^\eta$ , having a shallow slope  $\eta \sim -0.1$  for  $A_V < 3$  and very steep slope  $\eta \sim -2$  for  $A_V > 4$ . We then consider the effects of additional torques due to  $H_2$  formation and model grain alignment by joint action of RATs and  $H_2$  torques. We find that  $p/A_V$  tends to increase with an increasing magnitude of  $H_2$  torques. In particular, the theoretical predictions obtained for both  $p/A_V$  and peak wavelength  $\lambda_{\max}$  with both RATs and  $H_2$  formation better reproduce the observational data. Our results reinforce the predictive power of the RAT alignment mechanism in a broad range of environmental conditions and confirm the effect of pinwheel torques in environments with efficient  $H_2$  formation. Physical parameters involved in  $H_2$  formation may be constrained using detailed modeling of grain alignment combined with observational data. In addition, we discuss implications of our modeling for interpreting latest observational data by *Planck* and other ground-based instruments.

**Key words:** magnetic fields- polarization- dust, extinction

## 1 INTRODUCTION

Immediately after the discovery of polarization of light from distant stars, more than 60 years ago by [Hall \(1949\)](#) and [Hiltner \(1949\)](#), the polarization was attributed to differential extinction by non-spherical dust grains aligned with interstellar magnetic fields. This alignment of grains opened a new window into studying the magnetic fields, including the magnetic field strength through starlight polarization ([Davis & Greenstein 1951](#); [Chandrasekhar & Fermi 1953](#)) and polarized thermal dust emission ([Hildebrand 1988](#)), in various astrophysical environments. Moreover, polarized thermal emission from aligned grains is a significant Galactic foreground source contaminating cosmic microwave background experiments ([Dunkley et al. 2009](#); [Planck Collaboration et al. 2014a](#)). However, it is only recently that grain alignment theory has become quantitative and predictive, which allows for precision modeling of dust polarization and direct comparison with observations.

The problem of grain alignment has proven to be one of the longest standing problems in astrophysics. Over the last 60 years, a number of grain alignment mechanisms have been proposed and quantified (see [Lazarian 2007](#) for a review). Many substantially extending or modifying the initial paradigm of grain alignment based on the [Davis & Greenstein \(1951\)](#) paramagnetic relaxation theory. However, an alternative alignment paradigm, based on radiative alignment torques (RATs), has now become the favored mechanism to explain grain alignment. This mechanism was initially proposed by [Dolginov & Mitrofanov \(1976\)](#), but was mostly ignored at the time of its introduction due to the limited ability to generate quantitative theoretical predictions. [Draine & Weingartner \(1996\)](#) and [Draine & Weingartner \(1997\)](#) reinvigorated the study of the RAT mechanism by developing a numerical method based on discrete dipole approximation to compute RATs for several irregular grain shapes. The strength of the torques obtained made it impossible to ignore them, but questions about basic properties (e.g., direction, dependence on grain size and shape) of the alignment for grains of different shapes as well as degree of alignment remained.

\* E-mail: hoang@cita.utoronto.ca

The quantitative study of RAT alignment was initiated in a series of papers, by our group, starting with [Lazarian & Hoang \(2007a\)](#) (henceforth LH07) where an analytical model of RAT alignment was presented. The analytical model was the basis for further theoretical studies in ([Lazarian & Hoang 2007b](#); [Lazarian & Hoang 2008](#), [Hoang & Lazarian 2009b,a](#); see also reviews in [Lazarian 2007](#); [Lazarian, Andersson, & Hoang 2015](#); [Andersson, Lazarian, & Vaillancourt 2015](#)).

This work clarified why the grain alignment occurs with the long axes perpendicular to the magnetic field (as required by observations), even though the magnetic field provides only the axis of alignment, which earlier seemed to permit both the alignment perpendicular and parallel to the magnetic field. These studies opened a way for quantitatively predicting the grain alignment for a variety of astrophysical situations (see [Hoang & Lazarian 2014](#)).

The basic requirement for achieving grain alignment in the RAT paradigm is that grains with a net helicity are embedded in a magnetic field and exposed to anisotropic radiation with a wavelength less than the grain diameter. The radiation field also must have sufficient energy density. The grain's helicity causes a difference in the scattering cross section to the left- and right-hand circular polarization components of the radiation field, imparting a torque on the grain. As the grain gets magnetized through the Barnett effect ([Barnett 1915](#); [Dolginov & Mitrofanov 1976](#)), it Larmor precesses around the magnetic field lines. The continued action of the radiative torques on the spinning grain can then lead to alignment of grain angular momentum  $\mathbf{J}$  with the magnetic field  $\mathbf{B}$ .

In particular, we found that RATs tend to align grains at attractor points with low magnitude of angular momentum (i.e.,  $J \sim J_{\text{th}}$  with  $J_{\text{th}}$  being the thermal angular momentum, hereafter: low- $J$  attractor points), and/or attractor points with high angular momentum (i.e.,  $J > J_{\text{th}}$ , hereafter high- $J$  attractor points). The high- $J$  attractor points mostly correspond to perfect alignment of  $\mathbf{J}$  with  $\mathbf{B}$  (i.e.,  $\cos \beta = \pm 1$  with  $\beta$  the alignment angle made by  $\mathbf{J}$  and  $\mathbf{B}$ ), while the low- $J$  attractor points occur either at the perfect alignment angle or at some angle in the vicinity of the perfect alignment. The existence of high- $J$  attractor points depend on the angle between the radiation field anisotropy and the magnetic field, the grain shape and composition, and the radiation field. Within our analytical model (AMO) of RATs, the three latter parameters can be combined to a single parameter, which is the ratio of the RAT efficiency component parallel to the radiation field anisotropy direction to the component perpendicular to it. We expect reduced, i.e., of the order of 20-30 percent degree of alignment when the alignment happens at the low- $J$  attractor points. Both superparamagnetic inclusions and  $\text{H}_2$  formation torques had been considered as ways to increase the efficiency of paramagnetic alignment ([Jones & Spitzer 1967](#); [Purcell 1979](#); [Spitzer & McGlynn 1979](#)). It is interesting that both processes were found to be important for the RAT alignment.

We also found that the existence of strongly magnetic inclusions within the grain induces high- $J$  attractor points and thus make the alignment essentially perfect ([Lazarian & Hoang 2008](#)). In that sense, the inclusion of iron-rich clusters into dust grains can increase the fraction of grains aligned with high- $J$  attractor points. The dynamics of grain alignment is pretty complex with grains being moved by gas bombardment from the low- $J$  to high- $J$  attractor point and, paradoxically increasing the alignment in this way. In addition, grains undergo thermal flipping ([Lazarian & Draine 1999](#)).<sup>1</sup>

<sup>1</sup> The picture of thermal flipping was challenged by [Weingartner \(2009\)](#)

In addition to RATs, other uncompensated torques act on grains ([Purcell 1979](#); [Lazarian & Draine 1999](#)). [Purcell \(1979\)](#) proposed three processes that can produce uncompensated torques: hydrogen formation, photoelectric effect, and the variation of accommodation coefficient. [Hoang & Lazarian \(2009b\)](#) suggested the infrared emission from dust grains as another mechanism producing uncompensated torques. These pinwheel torques together with paramagnetic relaxation were at one time thought to be the major mechanism leading to the alignment of  $\mathbf{J}$  with  $\mathbf{B}$ . However, as shown by LH07, in the presence of RATs, the alignment arising from paramagnetic relaxation for ordinary paramagnetic grains is negligible compared to that arising from RATs.

Because the Purcell pinwheel torques ([Purcell 1979](#)) are fixed within the grain body, their efficiency in aligning the grains was found to decrease when the grains wobble rapidly and becomes negligible when the grain undergoes rapidly thermal flipping ([Lazarian & Draine 1999](#)). Nevertheless, in the framework of RAT alignment, the pinwheel torques were found to enhance the degree of grain alignment through two processes ([Hoang & Lazarian 2009b](#)). Firstly, when the grains are radiatively aligned with high- $J$  attractor points, the presence of  $\text{H}_2$  torques can enhance the degree of alignment by increasing the angular momentum of the high- $J$  attractor point, thus, driving some smaller grains to suprathreshold rotation (i.e. with rotation speeds well above the thermal energy of the environment). Secondly, for low- $J$  attractor points, the  $\text{H}_2$  torques can contribute to drive some grains that have sufficiently slow flipping (depending on their size) to suprathreshold rotation, i.e., creating new high- $J$  attractor points from low- $J$  attractor points. The latter corresponds to an increased fraction of grains aligned at high- $J$  attractor points compared to the case without  $\text{H}_2$  torques.

Grain alignment by RATs in molecular clouds has been studied by a number of authors ([Cho & Lazarian 2005](#); [Bethell et al. 2007](#); [Whittet et al. 2008](#); [Pelkonen et al. 2009](#); [Alves et al. 2014](#)). These studies dealt with the alignment of grains by the attenuated diffuse interstellar radiation field (ISRF). The observational data from [Whittet et al. \(2008\)](#) show that the fractional polarization can be described by a power-law,  $p_K/\tau_K \propto A_V^{-0.52 \pm 0.07}$ . A simple one-dimensional modeling of RAT alignment for a dense, uniform starless cloud presented in [Whittet et al. \(2008\)](#) finds that grains can still be aligned in the cloud interior with visual extinction  $A_V \sim 10$ . In addition, the modeling shows that the fractional polarization decreases slowly with  $A_V$  first (much shallower than  $A_V^{-0.52}$ ), and then it declines more rapidly as a power law  $A_V^{-1}$  starting from some large value of  $A_V$  (see [Whittet et al. 2008](#)). Very recently, [Jones et al. \(2014\)](#) report the results for  $p_K/\tau_K$  vs.  $A_V$  for starless cores with  $A_V$  up to 100 and found the trend  $p_K/\tau_K \propto A_V^{-1}$  as predicted, though at  $A_V \sim 20$ . It is noted that in the presence of magnetic turbulence, the fractional polarization for sightlines above the decorrelation length of magnetic fields is expected to be considerably reduced ([Jones et al. 1992](#)), which can also reproduce a power-law  $A_V^{-0.5}$  for  $A_V < 10$  as seen in [Whittet et al. \(2008\)](#), but the turbulence alone cannot reproduce the observational data for higher  $A_V$ . The importance of RAT alignment has also been shown for special (accretion disks, zodia-

who found that the grain does not experience thermal flipping as a result of internal relaxation, instead, it tends to be frozen at the separatrix (i.e., when the grain symmetry axis becomes perpendicular to the angular momentum). [Hoang & Lazarian \(2009b\)](#), however, showed that the excitation by gas bombardment and  $\text{H}_2$  formation can prevent the grain from being frozen at the separatrix. Thus, dust grains do flip.

cal cloud) and highly dynamic environments (e.g., cometary coma; see Hoang & Lazarian 2014 for more details).

Observational evidences for RAT alignment are numerous and increasingly available (Andersson & Potter 2007; Whittet et al. 2008; Andersson & Potter 2010; Matsumura et al. 2011; Andersson et al. 2011). In particular, fundamental features of RAT alignment such as the dependence of alignment on anisotropy direction of radiation, have been tested and confirmed by observations (see Andersson & Potter 2010; Andersson et al. 2011). However, evidence of enhancement of grain alignment by pinwheel torques has not been reported, until recently.

Very recent polarization observations of background stars behind the reflection nebula IC 63 by Andersson et al. (2013) show an enhancement in the polarization for those located behind some regions of the nebula with the strongest H<sub>2</sub> fluorescent intensity and an unusually steep dependence of  $p_V/A_V$  vs.  $A_V$ . Because hydrogen molecules cannot be photo dissociated by the general ISRF, the photo destruction of the H<sub>2</sub> molecule takes place in a two-step process. If, as an initial excitation into an upper electronic state of the molecule relaxes back to the electronic ground state, the molecule ends up in a vibrational state above  $v = 14$ , the molecule dissociates. Since the vibrational state population resulting from the electronic relaxation is determined by quantum mechanics, the fluorescent emission rate is directly proportional to the destruction rate of the molecule. If, as discussed in Andersson et al, the chemical time scales of the gas is much shorter than the macroscopic evolution time scales, then the destruction and reformation of the H<sub>2</sub> molecules will be in a state of detailed balance. This implies that the H<sub>2</sub> fluorescent intensity can be used as a tracer of the local H<sub>2</sub> formation rate.

Andersson et al. suggested the effect of additional torques from H<sub>2</sub> formations as a reason for the enhancement of  $p_V/A_V$  of the stars probing the high fluorescence regions. This paper is intended to present a detailed, ab-initio model of grain alignment by both RATs arising from stellar radiation of  $\gamma$  Cas as well as the attenuated ISRF and H<sub>2</sub> torques for the IC 63 nebula. Our results will be compared directly with the observational data, aiming to elucidate the role of RATs as well as H<sub>2</sub> torques on grain alignment.

Furthermore, given the moderate total column density of IC 63 (not deep enough to fully exclude the radiation field as discussed in Whittet et al. 2008), the steep decline of  $p_V/A_V$  seen in IC 63 cannot be explained by a low opacity RAT model with constant grain alignment and grain randomization. The observed slope is steeper than the standard predictions by RAT alignment for a starless cloud core in which grains are aligned by the attenuated ISRF. This paper also seeks to resolve this quandary.

The paper is organized as follows. In §2, we summarize the rotational damping processes and their characteristic timescales. A description of grain alignment by RATs and H<sub>2</sub> pinwheel torques is presented in §3. In §4 we describe a general method to model grain alignment by RATs and calculate linear polarization due to aligned grains. Principal results and comparison with observational data are presented in §5. Discussion and summary are presented in §6 and 7, respectively.

## 2 ROTATIONAL DAMPING

The rotational damping of interstellar grains mainly arises from collisions with gas atoms and from emission of infrared photons

(Purcell & Spitzer 1971; Roberge et al. 1993).<sup>2</sup> Below, their characteristic timescales are provided for reference.

### 2.1 Dust-Gas Collisions

Collisions of a grain with gas atoms consist of elastic collisions and sticking, inelastic collisions. In the latter regime, gas atoms temporally stick to the grain surface followed by their evaporation. For elastic collisions, and axisymmetric grain shape, the integration of all collisional torques over the grain surface tends to zero. In the grain frame of reference, the mean torque arising from the sticking collisions for the axisymmetric grain rotating around its symmetry axis also tends to zero when averaged over the grain revolving surface. On the other hand, the evaporation induces a non-zero mean torque, which is parallel to the rotation axis (see Roberge et al. 1993; Lazarian 1997).

To facilitate numerical estimates, we consider oblate spheroidal grains with moments of inertia  $I_1 > I_2 = I_3$  along the grain's principal axes  $\hat{\mathbf{a}}_1$ ,  $\hat{\mathbf{a}}_2$  and  $\hat{\mathbf{a}}_3$ . Let  $I_{\parallel} = I_1$  and  $I_{\perp} = I_2 = I_3$ . They take the following forms:

$$I_{\parallel} = \frac{2}{5} M a_2^2 = \frac{8\pi}{15} \rho a_1 a_2^4, \quad (1)$$

$$I_{\perp} = \frac{4\pi}{15} \rho a_1 a_2^2 (a_1^2 + a_2^2), \quad (2)$$

where  $a_1$  and  $a_2$  are the lengths of the semi-minor and semi-major axes of the oblate spheroid with inverse axial ratio  $s = a_1/a_2 < 1$ , and  $\rho$  is the density of grain material.

For the sake of consistency, we use the *effective* grain size  $a$ , which is defined as the radius of a sphere of equivalent volume as the following:

$$a = \left( \frac{3}{4\pi} (4\pi/3) a_1 a_2^2 \right)^{1/3} = a_2 s^{1/3}. \quad (3)$$

The rotational damping rate due to the dust-gas collisions is given by

$$\frac{\langle \Delta J \rangle}{\Delta t} = -\frac{J}{\tau_{\text{gas}}}, \quad (4)$$

where  $\tau_{\text{gas}}$  is the gaseous damping time:

$$\begin{aligned} \tau_{\text{gas}} &= \frac{3}{4\sqrt{\pi}} \frac{I_{\parallel}}{n_{\text{H}} m_{\text{H}} v_{\text{th}} a_2^4 \Gamma_{\parallel}}, \\ &= 6.58 \times 10^4 \hat{\rho} \hat{s}^{2/3} a_{-5} \left( \frac{100 \text{ K}}{T_{\text{gas}}} \right)^{1/2} \left( \frac{30 \text{ cm}^{-3}}{n_{\text{H}}} \right) \left( \frac{1}{\Gamma_{\parallel}} \right) \text{ yr}, \end{aligned} \quad (5)$$

where  $a_{-5}$  is the grain size in units of  $10^{-5}$  cm,  $\hat{s} = s/0.5$ ,  $\hat{\rho}$  is the grain material density in units of  $3 \text{ g cm}^{-3}$ . The thermal velocity of a gas atom of mass  $m_{\text{H}}$ , in a plasma with a temperature  $T_{\text{gas}}$  and density  $n_{\text{H}}$ , is  $v_{\text{th}} = (2k_{\text{B}}T_{\text{gas}}/m_{\text{H}})^{1/2}$ .  $\Gamma_{\parallel}$  is a geometrical parameter, which is equal to unity for spherical grains. This timescale is comparable to the time necessary for the grain to collide with an amount of gas equal to its own mass.

<sup>2</sup> Here we distinguish interstellar grains from polycyclic aromatic hydrocarbons (PAHs) with size less than  $100\text{\AA}$ . For PAHs, damping by additional processes, such as electric dipole emission, plasma drag, and ion collisions, can be important (Draine & Lazarian 1998; Hoang et al. 2010).

## 2.2 Infrared Emission

Photons emitted by the grain carry away part of the grain's angular momentum, resulting in damping of the grain rotation. The rotational damping rate by infrared emission can be written as

$$\tau_{\text{IR}}^{-1} = F_{\text{IR}} \tau_{\text{gas}}^{-1}, \quad (6)$$

where  $F_{\text{IR}}$  is the rotational damping coefficient for a grain of an equilibrium temperature  $T_d$  (see [Draine & Lazarian 1998](#)), which is given by

$$F_{\text{IR}} = \left( \frac{0.91}{a_{-5}} \right) \left( \frac{u_{\text{rad}}}{u_{\text{ISRF}}} \right)^{2/3} \left( \frac{30 \text{ cm}^{-3}}{n_{\text{H}}} \right) \left( \frac{100 \text{ K}}{T_{\text{gas}}} \right)^{1/2}. \quad (7)$$

where  $u_{\text{rad}}$  is the energy density of the radiation field and  $u_{\text{ISRF}} = 8.64 \times 10^{-13} \text{ ergs cm}^{-3}$  is the energy density of the average radiation field in the solar neighborhood as given by [Mezger et al. \(1982\)](#).

The total damping rate is then given by

$$\tau_{\text{drag}}^{-1} = \tau_{\text{gas}}^{-1} + \tau_{\text{IR}}^{-1} = \tau_{\text{gas}}^{-1} (1 + F_{\text{IR}}). \quad (8)$$

For large grains (i.e.,  $a > 0.1 \mu\text{m}$ ), the gaseous damping is dominant, and  $\tau_{\text{drag}} \approx \tau_{\text{gas}}$ . For small grains (i.e.,  $a \sim 0.01 \mu\text{m}$ ), the damping by infrared emission becomes dominant for most of the ISM, except for molecular clouds ([Draine & Lazarian 1998](#)).

Usually, we represent the grain angular momenta and time scales in units of the thermal angular momentum  $J_{\text{th}}$  and gaseous damping time  $\tau_{\text{gas}}$ . The former is given by

$$\begin{aligned} J_{\text{th}} &= \sqrt{I_{\parallel} k_{\text{B}} T_{\text{gas}}} = \sqrt{\frac{8\pi \rho s a_2^5}{15} k_{\text{B}} T_{\text{gas}}}, \\ &= 1.05 \times 10^{-19} \hat{s}^{-1/3} \hat{\rho}^{1/2} a_{-5}^{5/2} \left( \frac{T_{\text{gas}}}{100 \text{ K}} \right)^{1/2} \text{ g cm}^2 \text{ s}^{-1} \end{aligned} \quad (9)$$

## 3 GRAIN ALIGNMENT BY RADIATIVE TORQUES AND H<sub>2</sub> FORMATION TORQUES

Consider a grain subject to an external regular torque  $\mathbf{\Gamma}$  and a damping torque. The evolution of the grain angular momentum is then governed by the conventional equation of motion:

$$\frac{d\mathbf{J}}{dt} = \mathbf{\Gamma} - \frac{\mathbf{J}}{\tau_{\text{drag}}}, \quad (10)$$

where  $\tau_{\text{drag}}$  is the rotational damping time given by Equation (8).

The value of the grain's angular momentum in a stationary state, denoted by  $J_{\text{max}}$ , can be obtained by setting  $d\mathbf{J}/dt = 0$ , thus

$$J_{\text{max}} = \Gamma_J \times \tau_{\text{drag}}, \quad (11)$$

where  $\Gamma_J$  is the torque component projected onto the direction of  $\mathbf{J}$ .

### 3.1 Regular torques arising from H<sub>2</sub> formation

[Purcell \(1979\)](#) proposed a number of processes that can spin grains up to suprathermal rotation, including the formation of H<sub>2</sub> molecules over the grain surface, variation of accommodation coefficient (the density of sites of H<sub>2</sub> formation over the grain surface), and variations of the photoelectric emissivity. Among these processes, the formation of H<sub>2</sub> at catalytic sites on the grain surface, followed by the ejection of the H<sub>2</sub> molecule, was identified as a dominant mechanism.

Detailed calculations for the systematic torques for a brick-like and a spheroidal grain were presented in [Purcell \(1979\)](#), [Lazarian & Draine \(1997\)](#) and [Lazarian & Roberge \(1997\)](#), respectively. For a brick-like grain with sides  $2a_2$ ,  $2a_2$  and height  $2a_1$  considered in [Hoang & Lazarian \(2009b\)](#), the magnitude of torques due to H<sub>2</sub> formation that acts to spin the grain up along its symmetry axis takes the following form

$$\begin{aligned} \Gamma_{\text{H}_2} &= r^2 (r+1)^{1/2} \gamma_{\text{H}} (1-y) n_{\text{H}} \langle v_{\text{H}} \rangle (2a_1)^3 \left( \frac{2m_{\text{H}} E_{\text{kin}}}{3\nu} \right)^{1/2}, \\ &= \left( \frac{16}{3\pi} \right)^{1/2} r^2 (r+1)^{1/2} \gamma_{\text{H}} (1-y) n_{\text{H}} (2a_1)^3 (k_{\text{B}} T_{\text{gas}})^{1/2} \left( \frac{E_{\text{kin}}}{\nu} \right)^{1/2} \end{aligned} \quad (12)$$

where  $r = a_2/2a_1 = 1/2s$ ,  $1-y$  with  $y = 2n(\text{H}_2)/n_{\text{H}}$  is the fraction of atomic hydrogen,  $\gamma_{\text{H}}$  is the conversion efficiency from atomic to molecular hydrogen, and  $\langle v_{\text{H}} \rangle = (8k_{\text{B}} T_{\text{gas}} / \pi m_{\text{H}})^{1/2}$  is the mean speed of H atoms. Here  $\nu = \alpha \times 8r(1+r)(2a_1)^2$  is the number of active sites on the grain surface with  $\alpha$  the surface density of catalytic site, and  $E_{\text{kin}}$  is the mean kinetic energy of hydrogen molecules escaping from the grain surface (see Appendix B detailed derivation).

For the chosen brick, the effective grain size is given by  $4\pi/3a^3 = (2a_1)(2a_2)^2$ , and we get  $a_1 = a(\pi s^2/6)^{1/3}$ . Thus, Equation (B18) can be rewritten as

$$\begin{aligned} \Gamma_{\text{H}_2} &= \left( \frac{2}{3\pi} \right)^{1/2} \left( \frac{\pi}{6} \right)^{2/3} \left( \frac{s^{-1/3}}{8} \right)^{1/2} \\ &\quad \times \gamma_{\text{H}} (1-y) n_{\text{H}} (2a)^2 (k_{\text{B}} T_{\text{gas}})^{1/2} \left( \frac{E_{\text{kin}}}{\alpha} \right)^{1/2}. \end{aligned} \quad (13)$$

Using typical parameters one obtains

$$\Gamma_{\text{H}_2} = 1.89 \times 10^{-29} \hat{s}^{-1/6} \hat{\gamma}_{\text{H}} (1-y) \hat{n}_{\text{H}} \hat{T}_{\text{gas}}^{1/2} a_{-5}^2 \hat{E}_{\text{kin}}^{1/2} \hat{\alpha}^{-1/2} \text{ g cm}^2 \text{ s}^{-2}$$

where  $\hat{\gamma}_{\text{H}} = \gamma_{\text{H}}/0.2$ ,  $\hat{E}_{\text{kin}} = E_{\text{kin}}/0.2 \text{ eV}$ , and  $\hat{\alpha} = \alpha/10^{12} \text{ cm}^{-2}$ .

From Equations (11) and (13), we find the maximum angular momentum spun up by H<sub>2</sub> torques in units of  $J_{\text{th}}$ :

$$\begin{aligned} \frac{J_{\text{max}}^{\text{H}_2}}{J_{\text{th}}} &\approx 375.4 (1-y) \hat{\gamma}_{\text{H}} \hat{\rho}^{1/2} \hat{s}^{5/6} \hat{E}_{\text{kin}}^{1/2} \hat{\alpha}^{-1/2} \\ &\quad \times a_{-5}^{1/2} \hat{T}_{\text{gas}}^{-1/2} \left( \frac{1}{1 + F_{\text{IR}}} \right), \end{aligned} \quad (14)$$

where  $\tau_{\text{gas}}$  and  $J_{\text{th}}$  are given by Equations (5) and (9).

Equation (14) shows that H<sub>2</sub> torques increase with the decreased active site density  $\alpha$ . It means that fewer active sites correspond to stronger H<sub>2</sub> torques. This parameter is not well constrained at the moment.

[Lazarian \(1995\)](#) argued that, if there are a few active sites per grain, then the poisoning of active sites by O atoms dominates and is more important than the grain resurfacing, resulting in the suppression of H<sub>2</sub> torques. For  $T_d > 20 \text{ K}$ , he found that the mobility of O atoms leads to rapid poisoning of the active, chemisorption sites and hence produces short lived spin-up torques. However, more recent laboratory experiments on H<sub>2</sub> formation ([Pirronello et al. 1997, 1999](#)) indicate that, under cold interstellar conditions, it is dominated by physisorbed particles and is efficient only at  $T_d \sim 6-10 \text{ K}$  for olivine and 13-17 K for amorphous carbon ([Katz et al. 1999](#)). [Cazaux & Tielens \(2004\)](#) argued that at higher temperatures H atoms can access chemisorption sites, which would extend the H<sub>2</sub> formation to higher temperature (cf. [Cuppen & Herbst 2005](#)). Whether the physisorption sites can be localized enough to allow for long-lived "Purcell rockets" is not clear. If not, it might be that H<sub>2</sub> torques can only contribute significantly to grain alignment at

relatively high dust temperatures, even under the influence of active site poisoning. For the present analysis, we will assume that the formulation of, and constraints on, H<sub>2</sub> torques from Lazarian (1995) is valid. Therefore, small grains with few active sites are unlikely spun up to suprathermal rotation by H<sub>2</sub> torques.

Moreover, small grains are shown to undergo fast thermal flipping for which systematic torques fixed within the grain body are significantly reduced (see Lazarian & Draine 1999). Hoang & Lazarian (2009b) calculated the net pinwheel torques in the presence of thermal flipping and found that the net values are decreased by a reduction factor  $\Delta f$  (see their Figure 13), compared to the maximum value in Equation (14).

In particular, the magnitude of H<sub>2</sub> torques is determined by the fraction of atomic hydrogen,  $1 - y = n(\text{H})/n_{\text{H}}$ . The stationary fraction of atomic to molecular hydrogen is determined by the equilibrium between the formation and destruction of hydrogen molecule. The H<sub>2</sub> destruction is dominated by the photodissociation due to strong radiation fields from the star. As a result, in dense clouds, very low fraction of atomic hydrogen is expected, while in diffuse clouds, a significant fraction of atomic hydrogen is expected (Rachford et al. 2009).

### 3.2 Anisotropic Radiative Torques

Let  $u_{\lambda}$  be the energy density of radiation field per wavelength  $\lambda$  and  $\gamma_{\text{rad}}$  its anisotropy. Denote  $u_{\text{rad}} = \int u_{\lambda} d\lambda$ , which is the energy density of radiation. Radiative torque arising from the interaction of an anisotropic radiation field of direction  $\mathbf{k}$  with an irregular grain of size  $a$  is then given by

$$\Gamma_{\lambda} = \gamma_{\text{rad}} \pi a^2 u_{\lambda} \left( \frac{\lambda}{2\pi} \right) \mathbf{Q}_{\Gamma}, \quad (15)$$

where  $\mathbf{Q}_{\Gamma}$  is the RAT efficiency, which can be decomposed into three components  $Q_{e1}$ ,  $Q_{e2}$  and  $Q_{e3}$  in a scattering reference frame defined by unit vectors  $\hat{\mathbf{e}}_1, \hat{\mathbf{e}}_2, \hat{\mathbf{e}}_3$  with  $\hat{\mathbf{e}}_1 \parallel \mathbf{k}$ ,  $\hat{\mathbf{e}}_2 \perp \hat{\mathbf{e}}_1$  and  $\hat{\mathbf{e}}_3 = \hat{\mathbf{e}}_1 \times \hat{\mathbf{e}}_2$  (Draine & Weingartner 1996; Lazarian & Hoang 2007a).

In general, the magnitude of RAT efficiency  $Q_{\Gamma}$  depends on radiation field, grain shape, size and its orientation relative to  $\mathbf{k}$ . For the case in which the radiation direction is parallel to the axis of maximum moment of inertia  $\hat{\mathbf{a}}_1$ , LH07 found that the magnitude of RAT efficiency can be approximated by a power law as:

$$Q_{\Gamma} \approx 0.4 \left( \frac{\lambda}{a} \right)^{\eta}, \quad (16)$$

where  $\eta = 0$  for  $\lambda \lesssim 2a$  and  $\eta = -3$  for  $\lambda \gg a$ .

From Equations (11) and (16) one can then determine the maximum angular momentum induced by RATs as:

$$\begin{aligned} \frac{J_{\text{max}}^{\text{RAT}}}{J_{\text{th}}} &= \left( \int \Gamma_{\lambda} d\lambda \right) \frac{\tau_{\text{drag}}}{J_{\text{th}}}, \quad (17) \\ &\approx 200 \hat{\gamma}_{\text{rad}} \hat{\rho}^{1/2} a_{-5}^{1/2} \left( \frac{30 \text{ cm}^{-3}}{n_{\text{H}}} \right) \left( \frac{100 \text{ K}}{T_{\text{gas}}} \right) \\ &\quad \times \left( \frac{\bar{\lambda}}{1.2 \mu\text{m}} \right) \left( \frac{u_{\text{rad}}}{u_{\text{ISRF}}} \right) \left( \frac{\overline{Q_{\Gamma}}}{10^{-2}} \right) \left( \frac{1}{1 + F_{\text{IR}}} \right) \end{aligned} \quad (18)$$

where  $\hat{\gamma}_{\text{rad}} = \gamma_{\text{rad}}/0.1$ , and

$$\bar{\lambda} = \frac{\int \lambda u_{\lambda} d\lambda}{u_{\text{rad}}}, \quad (19)$$

$$\overline{Q_{\Gamma}} = \frac{\int Q_{\Gamma} \lambda u_{\lambda} d\lambda}{\bar{\lambda} u_{\text{rad}}}, \quad (20)$$

are the wavelength and RAT efficiency averaged over the entire radiation field spectrum, respectively.

Using Equations (16)-(20), we can calculate the maximum rotation rate  $J_{\text{max}}^{\text{RAT}}$  due to RATs for an arbitrary grain of size  $a$  embedded in a known radiation field  $u_{\lambda}$ .

The characteristic timescale for RATs to spin a thermally rotating grain to suprathermal velocity is defined as

$$\begin{aligned} \tau_{\text{spin-up}} &= \frac{J_{\text{th}}}{dJ/dt} = \frac{J_{\text{th}}}{\Gamma - J/\tau_{\text{drag}}} \\ &= \frac{\tau_{\text{drag}}}{J_{\text{max}}/J_{\text{th}} - 1}, \end{aligned} \quad (21)$$

where Equation (10) has been used.

The maximum angular momentum that the grain is spun up to, due to RATs and H<sub>2</sub> torques, depends on  $a$ ,  $u_{\text{rad}}$ , and  $\alpha$ . Thus, we can write

$$J_{\text{max}}(a, \bar{\lambda}, u_{\text{rad}}, \alpha, y) = J_{\text{max}}^{\text{RAT}}(a, \bar{\lambda}, u_{\text{rad}}) + J_{\text{max}}^{\text{H}_2}(\alpha, y) \Delta f, \quad (22)$$

where  $\Delta f$  accounts for the reduction of the pinwheel torques due to grain flipping (Hoang & Lazarian 2009b).

### 3.3 Dependence of RAT alignment on radiation direction

The maximum grain angular momentum induced by RATs,  $J_{\text{max}}^{\text{RAT}}$  (as given by Equation 18), is obtained assuming that  $\mathbf{k}$  is parallel to the grain axis of maximum moment of inertia  $\hat{\mathbf{a}}_1$  (i.e., the angle between  $\mathbf{k}$  and  $\hat{\mathbf{a}}_1$  is  $\Theta = 0$ ). In the presence of an ambient magnetic field, the grain usually rotates about the axis of alignment,  $\mathbf{B}$ . Thus, if  $\mathbf{k}$  is not parallel to  $\mathbf{B}$ , the actual value  $J_{\text{max}}^{\text{RAT}}$  is reduced due to projection effects.

Hoang & Lazarian (2009a) (HL09a) found that  $J_{\text{max}}^{\text{RAT}}$  decreases with an increasing angle  $\psi$  between  $\mathbf{k}$  and  $\mathbf{B}$ . Since the RAT alignment tends to occur with  $\mathbf{J}$  parallel (antiparallel) to  $\mathbf{B}$ , only the RAT component projected onto  $\mathbf{B}$  spins the grains up to a maximum angular momentum.

Using the analytical expressions of  $Q_{e1}$  and  $Q_{e2}$  from AMO for the default model with  $q^{\text{max}} \equiv Q_{e1}^{\text{max}}/Q_{e2}^{\text{max}} = 1.2$ , we obtain the following (see Appendix A for derivation):

$$J_{\text{max}}^{\text{RAT}}(\psi) = J_{\text{max}}^{\text{RAT}}(\psi = 0) \cos \psi, \quad (23)$$

where  $J_{\text{max}}^{\text{RAT}}(\psi = 0)$  is given by Equation (18).

From Equation (23) we can see that  $J_{\text{max}}^{\text{RAT}}(\psi = 90^\circ) = 0$ . However, this zero value is obtained for the case without internal thermal fluctuations (see Section 3.5). When such thermal fluctuations are taken into account, it is expected that  $J_{\text{max}}^{\text{RAT}}(\psi = 90^\circ) \sim J_{\text{th}}$ , i.e., grains rotate thermally regardless of radiation intensity (Hoang & Lazarian 2008).

In addition to dependence on  $\psi$ , the existence of high- $J$  attractor points depend on other parameters, including grain shape, size, and spectrum of the radiation field (see LH07a). Observational evidence supporting a dependence for the grain alignment on the angle  $\psi$  was reported in Andersson & Potter (2010) and Andersson et al. (2011).

### 3.4 Suprathermal rotation and critical size of aligned grains

In the framework of RAT alignment, some grains are aligned at high- $J$  attractor points with  $J_{\text{high},J} = J_{\text{max}}(\psi)$  given by Equation (18), whereas most grains are driven to low- $J$  attractor points having  $J_{\text{low},J} \sim J_{\text{th}}$ . The alignment of grains at high- $J$  attractor points is stable if grains rotate suprathermally, i.e.,  $J_{\text{max}}(\psi) \gg J_{\text{th}}$ . Using the Langevin equations to follow the

RAT alignment of grains in the presence of gaseous randomization, [Hoang & Lazarian \(2008\)](#) found that grains can have nearly stable alignment when  $J_{\max}(\psi)/J_{\text{th}} \approx 3$ .

Let  $a_{\text{ali}}$  be the critical size of aligned grains, which is defined as the critical size of suprathermal rotation at high- $J$  attractor points. Taking the usage of the condition for the stable alignment  $J_{\max}(\psi) \approx 3J_{\text{th}}$  for Equation (18), one can determine  $a_{\text{ali}}$  as a function of the environment parameters, including  $u_{\text{rad}}$ ,  $n_{\text{H}}$ , and  $T_{\text{gas}}$ . Since RATs increase rapidly with  $a$ , grains larger than  $a_{\text{ali}}$  would be suprathermally rotating, i.e.,  $J_{\max}(\psi) > 3J_{\text{th}}$ , which results in the perfect internal alignment of grain axes with the angular momentum.

### 3.5 Parameterizing Degree of RAT Alignment

Let  $Q_X = \langle G_X \rangle$  with  $G_X = [3 \cos^2 \theta - 1]/2$  be the degree of internal alignment of the grain axis of maximum moment of inertia  $\hat{\mathbf{a}}_1$  with  $\mathbf{J}$  and  $Q_J = \langle Q_J \rangle$  with  $G_J = [3 \cos^2 \beta - 1]/2$  be the degree of external alignment of  $\mathbf{J}$  with  $\mathbf{B}$ . Here  $\theta$  is the angle between  $\hat{\mathbf{a}}_1$  and  $\mathbf{J}$ , and the angle brackets denote the average over the ensemble of grains. The net degree of alignment of  $\hat{\mathbf{a}}_1$  with  $\mathbf{B}$ , namely the Rayleigh reduction factor, is defined as  $R(a) = \langle G_X G_J \rangle$ .

Small grains (e.g.,  $a < a_{\text{ali}}$ ) can be weakly aligned by paramagnetic relaxation with degree less than 5% for the typical interstellar magnetic fields ([Hoang et al. 2014](#)). Due to their low mass, small grains mostly produce starlight polarization at ultraviolet wavelengths and have a minor contribution for optical and near-IR starlight polarization. Therefore, we disregard the contribution of the small grains and set  $R(a < a_{\text{ali}}) = 0$ .

While the degree of RAT alignment of the  $a \geq a_{\text{ali}}$  grains is not yet available from ab-initio calculations, it can be represented through a set of parameters inferred from the RAT alignment theory. Let  $f_{\text{high}J}$  be the fraction of grains that are aligned at high- $J$  attractor points, hence the fraction of grains aligned at low- $J$  attractor points is  $1 - f_{\text{high}J}$ . Since grains at high- $J$  attractor points more likely have perfect alignment of  $\mathbf{J}$  with  $\mathbf{B}$ , we can write  $Q_J$  as the following:

$$Q_J = f_{\text{high}J} + (1 - f_{\text{high}J})Q_{J,\text{low}J}, \quad (24)$$

where  $Q_{J,\text{low}J}$  is the degree of external alignment of grains at low- $J$  attractors.

The Rayleigh reduction factor then becomes:

$$R(a) = \langle G_J G_X \rangle = f_{\text{high}J} + (1 - f_{\text{high}J})Q_{J,\text{low}J}Q_{X,\text{low}J}, \quad (25)$$

where we use the fact that the external alignment with high- $J$  attractors corresponds to perfect alignment of  $\hat{\mathbf{a}}_1$  with  $\mathbf{J}$ , i.e.,  $Q_{X,\text{high}J} = 1$ . Equation (25) can be further simplified using an upper limit  $Q_{J,\text{low}J} \sim 1$ . Here, the correlation of  $Q_X$  and  $Q_J$  is disregarded, which is minor for suprathermal grains (see [Roberge & Lazarian 1999](#)).

The degree of internal alignment,  $Q_{X,\text{low}J}$ , at the low- $J$  attractor points where the grain axes undergo strong thermal fluctuations due to the vibrational-rotational energy exchange (VRE) is calculated by

$$Q_{X,\text{low}J} = \int_0^\pi \frac{(3 \cos^2 \theta - 1)}{2} f_{\text{VRE}}(\theta, J_{\text{low}J}) \sin \theta d\theta, \quad (26)$$

$$f_{\text{VRE}}(\theta, J_{\text{low}J}) = \mathcal{Z} \exp \left( -\frac{J_{\text{low}J}^2}{2I_{\parallel} k_B T_d} [1 + (h - 1) \sin^2 \theta] \right), \quad (27)$$

is the distribution function of grain axis with respect to the angular momentum. Here  $\mathcal{Z}$  is a normalization factor, determined by setting  $\int_0^\pi f_{\text{VRE}} \sin \theta d\theta = 1$ , and  $h = I_{\parallel}/I_{\perp}$  (see [Lazarian & Roberge 1997](#)).

The exact value of  $J_{\text{low}J}$  is expected to depend on numerous parameters, including RATs, grain temperature, and gas temperature. Thus, we take an upper value  $J_{\text{low}J} = J_{\text{th}}$ , which corresponds to the thermal equilibrium between gas randomization and grain rotation. Using Equation (26) we obtain  $Q_{X,\text{low}J}(J_{\text{th}}) \approx 0.084$  for oblate grain of  $s = 0.5$  and  $h = 1.6$ . We will see later that  $f_{\text{high}J}$  must be  $\geq 0.5$  to reproduce observations for IC 63. In this case, reducing  $J_{\text{low}J}$  from the upper value  $J_{\text{th}}$  only changes the total degree of alignment  $R$  by less than 10% because  $Q_{X,\text{low}J}$  is much smaller than the first term.

As shown in Equation (25), the most important parameter in polarization modeling by RATs is the fraction of grains aligned with high- $J$  attractor points,  $f_{\text{high}J}$ . LH07 showed that  $f_{\text{high}J}$  depends on numerous physical parameters, including the grain size  $a$ , grain shape,  $q^{\text{max}}$ , anisotropic direction of radiation  $\psi$  relative to the magnetic field, and radiation spectrum. For silicate of normal paramagnetism, the RAT alignment tends to have  $f_{\text{high}J} < 1$ . In the case of RAT alignment with high- $J$  attractor points,  $f_{\text{high}J}$  perhaps achieves unity (i.e., perfect alignment) when collisional pumping by gas collisions is taken into account. Nevertheless, the RAT alignment with high- $J$  attractors is not universal. It was also found that  $f_{\text{high}J}$  can be significantly increased when the ordinary paramagnetic grain has the inclusion of clusters of iron atoms ([Lazarian & Hoang 2008](#)). Therefore, we will not attempt to compute exact values of  $f_{\text{high}J}$  but treat it as a model parameter throughout this paper.

### 3.6 Theoretical Consideration for Effects of H<sub>2</sub> Torques

To better understand the effects of H<sub>2</sub> torques on the RAT alignment, let us consider the typical regime of RAT alignment with high- $J$  and low- $J$  attractor points.

For the alignment at high- $J$  attractor points, if RATs are strong, small grains  $a \leq 0.05 \mu\text{m}$  can still rotate suprathermally. Thus, the effect of H<sub>2</sub> torques for these small grains is minor because the rapid flipping of small grains act to significantly suppress H<sub>2</sub> torques ([Lazarian & Draine 1999](#)). For weak RATs, only large grains (e.g.,  $a > a_{\text{ali}} \sim 0.1 \mu\text{m}$ ) can rotate suprathermally, whereas intermediate grains (i.e.,  $a \sim 0.05 - 0.1 \mu\text{m}$ ) undergo slow flipping ([Lazarian & Draine 1999](#); [Hoang & Lazarian 2009b](#)). In this case, the presence of H<sub>2</sub> torques helps to drive some intermediate grains to suprathermal rotation, which results in the decrease of  $a_{\text{ali}}$  (i.e., smaller grains can still be aligned).

For the alignment at low- $J$  attractor points, it is noted that the spin-up component of RATs is negative in the vicinity of these attractor points, which tends to drive grains to thermal rotation. For  $a \gg a_{\text{ali}}$ , the flipping is expected to be slow, and H<sub>2</sub> torques tend to increase the angular momentum of the low- $J$  attractor points. In this case, a new high- $J$  attractor point will be produced if H<sub>2</sub> torques are sufficiently strong to counter the negative spin-up component of RATs ([Hoang & Lazarian 2009b](#)). Therefore, the presence of sufficiently strong H<sub>2</sub> torques tends to increase the fraction of grains with high- $J$  attractor points,  $f_{\text{high}J}$ .

In summary, the inclusion of H<sub>2</sub> torques is expected to result in (i) the decrease of  $a_{\text{ali}}$  and (ii) the increase of  $f_{\text{high}J}$ . The new value  $a_{\text{ali}}$  in the presence of H<sub>2</sub> torques can be easily calculated as in §3.4. To evaluate the increase of  $f_{\text{high}J}$  with H<sub>2</sub> torques, first we compute the rotation rate of grains at low- $J$  attractor points

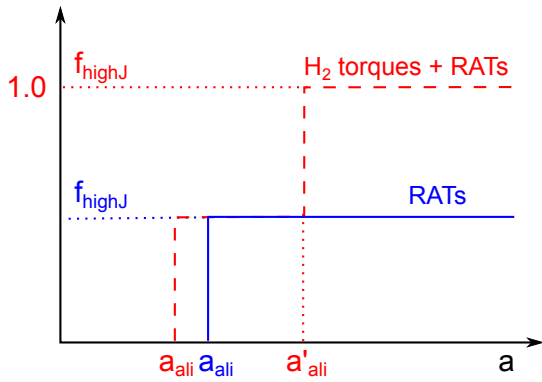


**Figure 1.** Illustration of the variation of the fraction of grains aligned on high- $J$  attractor points  $f_{\text{high},J}$  with grain size  $a$  for the alignment by RATs (solid line) and by both  $\text{H}_2$  torques and RATs (dashed line). Grains larger than  $a_{\text{ali}}$  are aligned with a fraction  $f_{\text{high},J}$  on high- $J$  attractor points. The effects of an additional  $\text{H}_2$  torque are to reduce  $a_{\text{ali}}$  of grains aligned at high- $J$  and increase  $f_{\text{high},J}$  to unity for  $a \geq a'_{\text{ali}}$ .

through Equation (37) in Hoang & Lazarian (2009b), which takes into account the reduction of RATs due to thermal fluctuations and grain flipping. Then, we calculate the minimum size of grains from the low- $J$  attractors that rotate suprathermally,  $a'_{\text{ali}}$ . Therefore, grains with  $a > a'_{\text{ali}}$  should rotate suprathermally, and we assume  $f_{\text{high},J}(a > a'_{\text{ali}}) = 1$ . Grains with  $a_{\text{ali}} < a < a'_{\text{ali}}$  still rotate thermally at low- $J$  attractor points. Stronger  $\text{H}_2$  torques tend to result in smaller  $a'_{\text{ali}}$ , which corresponds to a higher degree of alignment ( $f_{\text{high},J}$ ). The variation of  $f_{\text{high},J}$  with  $a$  can be summarized in Figure 1 for the RAT alignment without and with  $\text{H}_2$  torques.

#### 4 QUANTITATIVE MODELING OF RAT ALIGNMENT AND DUST POLARIZATION

In this section, we describe the general steps taken to model grain alignment in a molecular cloud induced by RATs plus  $\text{H}_2$  formation torques, and to predict linear polarization of light from background stars by aligned grains.

##### 4.1 Physical Model of IC 63 and Model Set up

Let us consider an idealized model of the IC 63 nebula, which can be approximated as a spherical cloud of uniform gas density of radius  $r_c$ . The nebula is illuminated by the star  $\gamma$  Cassiopeia located at projected distance  $d_{*,\text{sky}} = 1.3$  pc from the star and the attenuated ISRF. Physical parameters adopted for IC 63, including gas density  $n(\text{H}_2)$ , temperature  $T_{\text{gas}}$ , dust temperature  $T_{\text{d}}$  (Jansen et al. 1994; Jansen et al. 1996; France et al. 2005) and the parameters of  $\gamma$  Cas are listed in Table 1.

Based on the geometry of the diffuse emission, Andersson et al. (2013) found that IC 63 and  $\gamma$  Cas are offset from each other along the line of sight, with the line between  $\gamma$  Cas and IC 63 making an angle of  $\gamma_* = 58^\circ$  with respect to the plane of the sky (henceforth POS). The actual distance from  $\gamma$  Cas to IC 63 is  $d_* = d_{*,\text{sky}} / \cos(58^\circ) = 2.45$  pc. In addition, both the position angles of the optical polarization in the nebula and synchrotron measurements in the area encompassing IC 63 (Sun et al. 2007) show a projected magnetic field closely parallel to the Galactic plane. While direct determinations of the three dimensional structure of the magnetic field in the region are

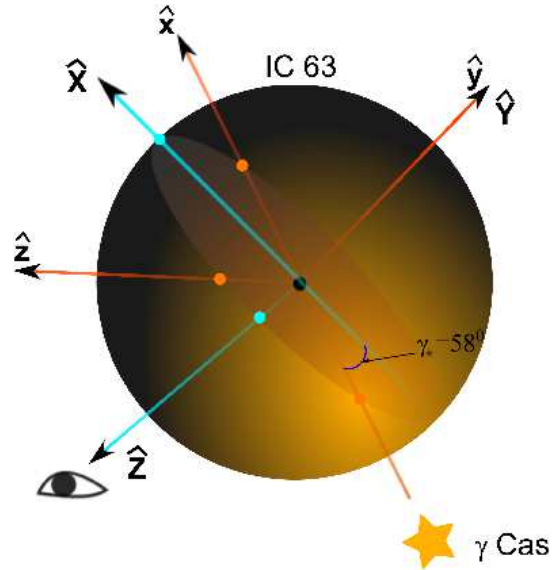


**Figure 2.** 3D schematic illustration of the IC 63 nebula and the  $\gamma$  Cas star, and coordinate systems defined for calculations.  $\hat{\mathbf{Z}}$  denotes the line of sight toward background stars, and the  $\hat{\mathbf{X}}\hat{\mathbf{Y}}$  plane, perpendicular to  $\hat{\mathbf{Z}}$ , describes the plane of the sky. The  $\gamma$  Cas star illuminates IC 63 in the  $\hat{\mathbf{x}}$  direction, which is along the path connecting the star and nebula, and the star-nebula-path makes an angle  $\gamma_* = 58^\circ$  with the POS  $\hat{\mathbf{X}}\hat{\mathbf{Y}}$ . The  $\hat{\mathbf{x}}\hat{\mathbf{z}}$  plane with  $\hat{\mathbf{z}} \perp \hat{\mathbf{x}}$  describes a cut through the nebula containing the star-nebula path and perpendicular to the POS. The cyan and orange filled circles denote the intersections of the vectors with the nebula.

**Table 1.** Physical parameters for the IC 63 nebula

Parameters	Values
Nebula radius, $r_c$	0.03 pc
$n(\text{H}_2)$	$2 - 4 \times 10^4 \text{ cm}^{-3}$
$n(\text{H})/2n(\text{H}_2)$ near surface	0.1 <sup>a</sup>
$T_{\text{gas}}$	150 K
$T_{\text{d}}$	45 K
$\gamma$ Cas	B0.5 IV
Nebula- $\gamma$ Cas projected distance, $d_{*,\text{sky}}$	1.3 pc
$R_*$	$14R_{\odot}$
$T_*$	30500 K
Distance of the star, D	200 pc
$\text{H}_2$ formation efficiency, $\gamma_{\text{H}}$	0.1

<sup>a</sup> see France et al. (2005).

not available, we can estimate the over-all field orientation by assuming that it follows the spiral arms. If we use a pitch angle for the local and Persus arms of  $\sim 10^\circ$  (Xu et al. 2013), and the Galactic longitude for IC 63 of  $l=163^\circ$ , we find that the magnetic field makes an angle of  $\sim 43^\circ$  with the line of sight (or an angle  $\xi = 47^\circ$  with the POS).

For our modeling, we define two coordinate systems centered in IC 63,  $\hat{\mathbf{x}}\hat{\mathbf{y}}\hat{\mathbf{z}}$  and  $\hat{\mathbf{X}}\hat{\mathbf{Y}}\hat{\mathbf{Z}}$  with  $\hat{\mathbf{y}} \equiv \hat{\mathbf{Y}}$ , where the  $\hat{\mathbf{X}}\hat{\mathbf{Y}}\hat{\mathbf{Z}}$  coordinate system is obtained by rotating the  $\hat{\mathbf{x}}\hat{\mathbf{y}}\hat{\mathbf{z}}$  system by an angle  $\gamma_*$  around the  $\hat{\mathbf{Y}}$  axis (see Figure 2).

## 4.2 Simplified Radiative transfer

Dust grains inside IC 63 are illuminated both by stellar radiation from  $\gamma$  Cas as well as the attenuated interstellar radiation field (ISRF). We adopt the ISRF spectrum  $u_\lambda$  (ISRF) from Mathis et al. (1983) and assume a degree of anisotropy  $\gamma_{\text{rad}} = 0.35$  as numerically calculated in (Bethell et al. 2007). The stellar radiation from  $\gamma$  Cas is completely anisotropic with  $\gamma_{\text{rad}} = 1$ . Since the distance between the star and nebula is much larger than the nebula's radius, the incident stellar radiation can be approximated as parallel beams.

For convenience, we begin with a slab  $\hat{x}\hat{z}$  of  $y=0$  as shown in Figure 3, which contains both the IC 63- $\gamma$  Cas connecting line and perpendicular to the POS. Let  $\tau_x$  be the optical depth for the extinction of the stellar radiation by dust along the  $\hat{x}$  direction. We divide the  $\hat{x}\hat{z}$  plane into  $N_x \times N_z$  cells with  $N_x = N_z = 128$ . The gas density, temperature, and density of radiation energy at each cell are given by  $n_{\text{H}}(x, z)$ ,  $T_{\text{gas}}(x, z)$ , and  $u_\lambda(x, z)$ , respectively.

Provided the effective temperature  $T_\star$  of  $\gamma$  Cas and the distance  $d_\star$  from the star to IC 63, we can derive the spectral energy density  $u_\lambda$  as follows:

$$u_\lambda = \frac{4\pi}{c} \frac{\int I_\lambda d\Omega}{4\pi}, \quad (28)$$

where  $I_\lambda$  is the intensity of radiation (assuming a black body spectrum) and  $\Omega$  is the solid angle subtended by the star at the distance for IC 63, in steradians. For isotropic radiation from the star  $I_\lambda = B_\lambda(T_\star)$ . Due to the extinction by dust, the energy density decreases with optical depth as

$$u_\lambda = \frac{\pi B_\lambda(T_\star)}{c} \left(\frac{R_\star}{d_\star}\right)^2 e^{-\tau_x(\lambda)} + u_\lambda(\text{ISRF})e^{-\tau_{\text{sd}}(\lambda)}, \quad (29)$$

where the reemission of dust with temperature  $T_{\text{d}} = 45$  K (see Table 1) in infrared is ignored because the RAT efficiency  $Q_{\text{r}} decreases substantially at infrared wavelengths  $\lambda \gg a$ , and the second term denotes the attenuated ISRF, which is subdominant for the conditions of IC 63 (see Eq. 18). Above  $\tau_{\text{sd}}$  is the optical depth along the anisotropic direction of the ISRF, which only depends on the distance (i.e., extinction) from the cloud surface to the position of dust grains.$

The optical depth by a dust column of thickness  $dx$  along the  $\hat{x}$  axis is given by

$$d\tau_x(\lambda) = \int_{a_{\text{min}}}^{a_{\text{max}}} C_{\text{ext}}(\lambda, a) \left(\frac{dn}{da}\right) da, \quad (30)$$

where  $C_{\text{ext}} = (2C_\perp + C_\parallel)/3$  is the extinction cross-section due to randomly oriented grains (see Appendix C), and  $dn/da$  is the grain size distribution. Here, the integration over the grain size is carried out for both silicate and carbonaceous grains. By convention,  $C_\parallel$  and  $C_\perp$  are the extinction cross-section for the electric field of incident radiation parallel and perpendicular to the grain symmetry axis, respectively.

Using the physical parameters for IC 63 in Table 1 for Equations (30), one can calculate the optical depth as a function of wavelength. With  $\tau_x$  known, one can calculate  $u_\lambda$  inside the nebula using Equation (29). The total energy density is obtained by integrating  $u_\lambda$  over the entire spectrum of the stellar radiation field, i.e.,  $u_{\text{rad}}(x, z) = \int u_\lambda d\lambda$ .

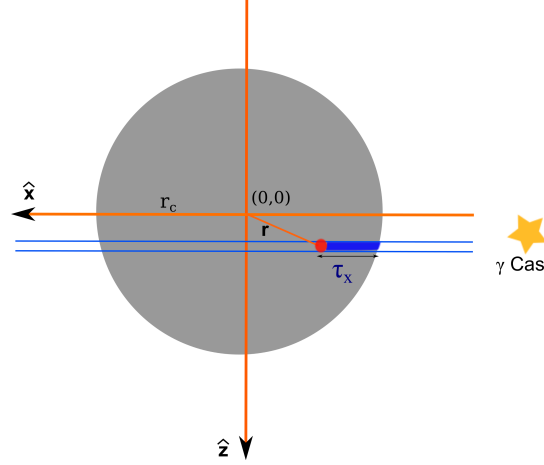


**Figure 3.** Schematic of grain alignment in a circular slab  $\hat{x}\hat{z}$  with  $y=0$  (middle slab) by the stellar radiation from  $\gamma$  Cas.  $r$  is the distance from the grain to the center of IC 63 and  $\tau_x$  is the optical depth with respect to  $\gamma$  Cas. The positive direction of  $x$  is chosen along the direction of light propagation. Dayside and nightside have  $x < 0$  and  $x > 0$ , respectively.

## 4.3 Critical size of aligned grains

Using  $u_{\text{rad}}(x, z)$  for Equations (22)-(23), one obtains  $J_{\text{max}}/J_{\text{th}}$  due to RATs and  $\text{H}_2$  torques. The critical size of aligned grains,  $a_{\text{ali}}(x, z)$ , can be evaluated using the criteria in Section 3.

## 4.4 Linear Polarization

Consider a column of dust along the  $\hat{Z}$  axis toward a background star with the visual extinction  $A_V = 1.086\tau_Z(\lambda = 0.55 \mu\text{m})$ , where  $\tau_Z$  is obtained by integrating Equation (30) along the  $\hat{Z}$  axis. It is noted that the sightlines toward background stars, parallel to the  $\hat{Z}$  axis, make an angle  $\gamma_\star$  with the  $\hat{z}$  axis (see Figure 2).

The degree of linear polarization arising from the aligned asymmetric silicate grains in a cell of thickness  $dZ$  is computed as the following:

$$dp_\lambda(X, Z) = \int_{a_{\text{ali}}(X, Z)}^{a_{\text{max}}} \frac{(C_X - C_Y)}{2} \frac{dn}{da} da dZ, \quad (31)$$

where  $a_{\text{ali}}(X, Z)$  is the critical size of aligned grains in the cell  $(X, Z)$  (see Appendix D for derivation).

The value  $a_{\text{ali}}(X, Z)$  in the  $XZ$  grid is interpolated from  $a_{\text{ali}}(x, z)$  with the use of the coordinate transformation from  $\hat{x}\hat{z}$  to  $\hat{X}\hat{Z}$  coordinate systems.

As shown previously (Hoang et al. 2013, 2014), small grains have very low, but finite residual alignment degree. However, they only affect starlight polarization in the ultraviolet wavelengths, whereas the peak of polarization spectrum is mostly determined by aligned large grains. Thus, the minor contribution of  $a < a_{\text{ali}}$  grains is disregarded in the above equation.

Equation (31) can be rewritten as

$$dp_\lambda(X, Z) = \int_{a_{\text{ali}}(X, Z)}^{a_{\text{max}}} \frac{C_{\text{pol}}}{2} R(a) \cos^2 \xi \frac{dn}{da} da dZ, \quad (32)$$

where  $C_{\text{pol}} = (C_\parallel - C_\perp)$  is the polarization cross-section for oblate spheroidal grains,  $\xi$  is the angle between the magnetic field and the POS, and  $R(a)$  is given by Equation (25).

Equations (32) is integrated over  $Z$  to obtain the polarization  $p_\lambda(X)$  for each line of sight (i.e.,  $A_V$ ) with the use of the step



function  $f_{\text{high},J}$  from Figure 1. The transition of alignment from unaligned, small grains to aligned grains at  $a = a_{\text{ali}}$  is unlikely a sudden jump (see e.g. Hoang et al. 2014), and we multiply  $R(a)$  by a smoothing function  $f_{\text{sm}} = 1 - \exp[-(a/a_{\text{ali}})^3]$ .

The extinction cross-section  $C_{\text{ext}}$  and polarization cross-section  $C_{\text{pol}}$  are taken from Hoang et al. (2013) who computed the cross-sections for silicate and carbonaceous grains with the dielectric functions from Draine (2003). Oblate spheroidal grains of axial ratio  $r = 2$  are considered.

## 5 RESULTS

In this section, we present predictions for grain alignment and polarization, assuming a mixture model of dust consisting of amorphous silicate grains and carbonaceous grains. The grain size distributions are taken from the model with a typical total-to-selective extinction  $R_V = 3.1$  for the ISM from Weingartner & Draine (2001), in which the distribution for silicate has a sharp decline at  $a_{\text{max}} \sim 0.25 \mu\text{m}$ . Photometric analysis in Andersson et al. (2013) shows that  $R_V$  varies across IC 63 with an averaged value  $\langle R_V \rangle = 2.27$ , which is smaller than the adopted  $R_V$ . For the calculations in this paper, the carbonaceous grains are assumed to be unaligned and thus to not contribute to the polarization (Chiar et al. 2006). In the following, we calculate the linear polarization for four different cloud models with gas density  $n(\text{H}_2) = 5 \times 10^4 \text{ cm}^{-3}$  (model 1),  $4 \times 10^4 \text{ cm}^{-3}$  (model 2),  $3 \times 10^4 \text{ cm}^{-3}$  (model 3) and  $2 \times 10^4 \text{ cm}^{-3}$  (model 4). Results presented here are calculated for  $f_{\text{high},J}^{\text{RAT}} = 0.5$ , i.e., 50% of grains are radiatively aligned with high- $J$  attractor points. We first consider the grain alignment solely by RATs, and subsequently consider the effects of the addition of  $\text{H}_2$  formation torques.

### 5.1 Grain Alignment by RATs

#### 5.1.1 Two-dimensional case

##### (a) Isothermal cloud model

Let us consider an isothermal cloud of gas temperature  $T_{\text{gas}} = 150 \text{ K}$  (see Table 1). We present results for grain alignment in a circular slab  $\hat{x}\hat{z}$  ( $\hat{X}\hat{Z}$ ) at  $y = 0$  (middle slab through the IC 63 center) considered in the previous section. Due to the effect of radiative transfer that directly illuminate grains in the slab, this realization corresponds to optimal alignment and polarization.

Figure 4 (upper panel) shows contours of the critical size of aligned grains  $a_{\text{ali}}$  induced by RATs only. As shown, in the region facing toward  $\gamma \text{ Cas}$  (hereafter dayside), which are directly illuminated by stellar radiation, grains as small as  $a \sim 0.06 \mu\text{m}$  can be aligned. In the region facing away from  $\gamma \text{ Cas}$  (hereafter nightside), only big grains  $a > 0.1 \mu\text{m}$  can be aligned. The critical size  $a_{\text{ali}}$  exceeds the assumed upper size cut-off ( $a_{\text{max}} \sim 0.25 \mu\text{m}$ ) of the grain distribution, and hence no aligned grains are predicted to be present, except very thin outer layer in which the attenuated ISRF has some effect. That is a direct consequence of the weakening of RATs due to the extinction of stellar radiation while propagating deeper into the nebula.

It is useful to define a column of aligned grains, which is a column of dust that contains all aligned grains with size  $a_{\text{ali}} \leq a_{\text{max}}$ . From Figure 4 (upper panel), one can see that, for the sightlines passing the region of aligned grains with  $X \leq -0.3$ , the column density of aligned grains increases with increasing total dust column density. Beyond  $X \sim -0.3$ , the column density of aligned

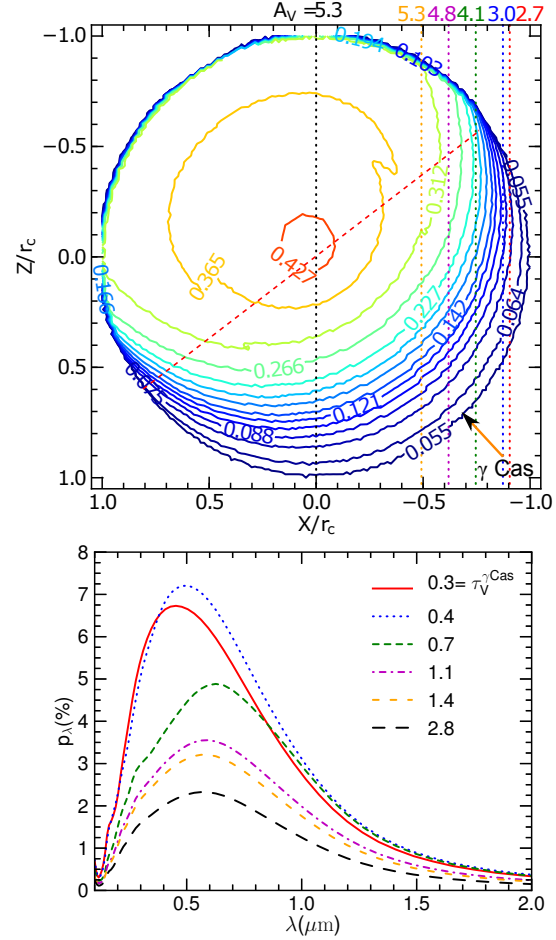


**Figure 4.** Upper panel: contours of  $a_{\text{ali}}$  in microns in the  $\hat{X}\hat{Z}$  plane for model 3 with  $n(\text{H}_2) = 3 \times 10^4 \text{ cm}^{-3}$ . Stellar radiation arrives from  $\gamma \text{ Cas}$  in the  $\hat{x}$  direction (marked by arrow) that makes an angle  $\gamma_* = 58^\circ$  with  $\hat{X}$ . Dashed diagonal line divides the dayside and nightside. Grains are efficiently aligned in the outer layer of the dayside that face  $\gamma \text{ Cas}$ , and only very large grains can be aligned in the nightside. Dotted lines show several sightlines toward background stars with  $A_V$  indicated. Grain alignment by only RATs is considered. Lower panel: polarization curves due to aligned grains by RATs along the selected sightlines shown in the upper panel. The V-band optical depths relative to  $\gamma \text{ Cas}$  in the  $\hat{X}$  direction,  $\tau_V^{\gamma \text{ Cas}}$ , are indicated for the selected sightlines. Grain alignment by only RATs for model 3 is considered.

grains decreases with increasing the total column density. Here the line of sight  $X \sim -0.3$  touches the contour  $a_{\text{ali}} \sim a_{\text{max}}$ .

Figure 4 (lower panel) shows the polarization curves calculated for the five sightlines through the dayside of the nebula with  $X \approx -0.9, -0.87, -0.75, -0.6, -0.5$  and  $X = 0$ . For model 3, the visual extinctions of these lines of sight are  $A_V = 2.7, 3.0, 4.1, 4.8, 5.3$  and  $6.1$ . The corresponding V-band optical depths in the direction to  $\gamma \text{ Cas}$  are  $\tau_V^{\gamma \text{ Cas}} = 0.3, 0.4, 0.7, 1.1, 1.5$  and  $2.8$  (see Eq. E2). First, the peak polarization increases with the increasing optical depth up to  $\tau_V^{\gamma \text{ Cas}} = 0.4$ , and then it substantially decreases for  $\tau_V^{\gamma \text{ Cas}} > 0.4$ . This can be easily understood. Indeed, Figure 4 (upper panel) shows that the sightlines  $X = -0.9$  ( $\tau_V^{\gamma \text{ Cas}} = 0.4$ ) and  $X = -0.75$  ( $\tau_V^{\gamma \text{ Cas}} = 0.7$ ) go through the region with most grains aligned (i.e.,  $a_{\text{ali}} < 0.1$ ) while the other two sightlines go through the region with only large grains aligned

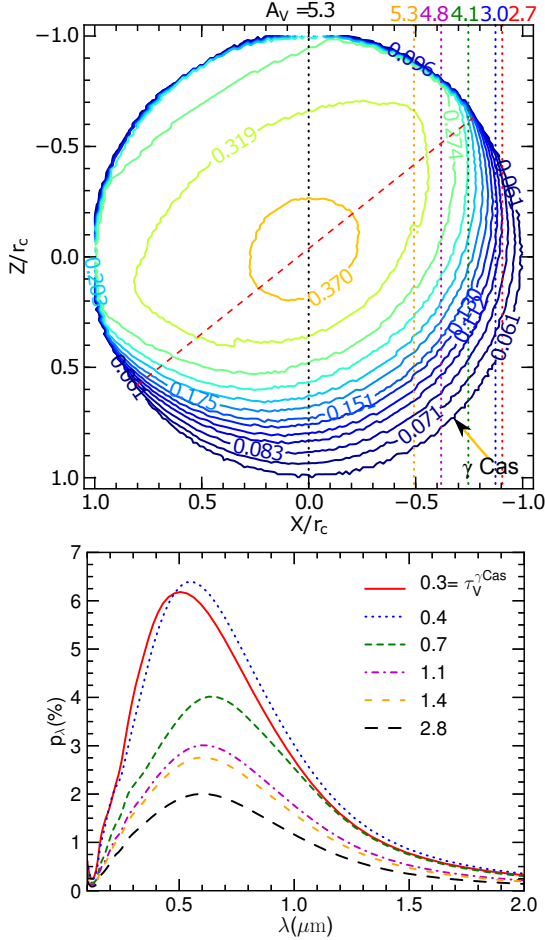


**Figure 5.** Similar to Figure 4, but for the case the gas temperature  $T_{\text{gas}}$  varies with the depth in the cloud characterized by  $\tau_V^{\gamma\text{Cas}}$ .

(i.e.,  $a_{\text{ali}} > 0.1$  for large  $Z$  only). The wavelength at which the polarization peaks,  $\lambda_{\text{max}}$ , increases with the increasing  $\tau_V^{\gamma\text{Cas}}$ .

(b) *Effects of gas temperature variation*

To evaluate the effects of gas temperature variation within the nebula and the resultant variable collision rate of grain alignment, we reran our models with the temperature profile obtained from a two-dimensional model in [Jansen et al. \(1995\)](#). Specifically, they show a decrease in the gas temperature,  $T_{\text{gas}}$ , with increasing optical depth in the direction of the stellar radiation (i.e., going deeper into the nebula). For instance, the temperature as high as  $T_{\text{gas}} \sim 250$  K is found at  $\tau_V^{\gamma\text{Cas}} \sim 0.2$  (i.e., in the cloud surface facing  $\gamma$  Cas) and falls to  $T_{\text{gas}} \sim 100$  K at  $\tau_V^{\gamma\text{Cas}} \sim 1.6$  and  $T_{\text{gas}} \sim 45$  K at  $\tau_V^{\gamma\text{Cas}} \sim 3.0$ . A high gas temperature close to the cloud surface facing  $\gamma$  Cas is directly supported by the  $\text{H}_2$  excitation measurements of [Fleming et al. \(2010\)](#).

Figure 5 (upper panel) shows the contours of  $a_{\text{ali}}$  in the presence of gas temperature variation. Compared to the results for isothermal case in Figure 4 (upper panel),  $a_{\text{ali}}$  increases in the outer layer but decreases in the inner region.

Figure 5 (lower panel) shows the polarization curves for the case where the spatial dependence of  $T_{\text{gas}}$  has been included. For sightlines close to the surface, the value  $p_{\text{max}}$  is decreased by a factor of 1.1, compared to the isothermal model, while for the inner sightline it has been increased by the comparable factor. The wavelength  $\lambda_{\text{max}}$  is increased in the former cases and decreased in

the latter. These results are easy to understand, as the regions with enhanced gas temperatures have stronger collisional damping and hence lower polarization than the results for the constant gas temperature. Meanwhile, the sightline  $\tau_V^{\gamma\text{Cas}} = 1.5$  now mostly probes a region with a lower temperature  $T_{\text{gas}} \sim 50$  K, corresponding to a weaker collisional damping, for which the grain alignment and polarization are increased.

(c) *Variation of  $p/A_V$  from the IC 63 edge to center*

Figure 6 shows the variation of fractional polarizations,  $p_{\text{max}}/A_V$  (left) and  $p_V/A_V$  (right), with  $A_V$ , calculated for the four models of IC 63. The variation of  $p_{\text{max}}/A_V$  with  $A_V$  essentially follows two separate stages, which can be well described by power law  $A_V^\eta$ . In the first stage,  $p_{\text{max}}/A_V$  decreases slowly with  $A_V$  with a shallow slope  $\eta \sim -0.2$ . In the second stage, it declines more rapidly, with a very steep slope  $\eta \sim -2$ . The variation of  $p_V/A_V$  versus  $A_V$  is similar to that of  $p_{\text{max}}/A_V$  in the second stage, but it is slightly shallower in the first stage, with  $p_V/A_V \propto A_V^{-0.1}$ .

The transition between two stages with the shallow and steep slopes occurs at visual extinction  $A_V^{\text{tr}}$ . This transition value tends to decrease with decreasing the gas density. For instance,  $A_V^{\text{tr}} \sim 4$  for  $n(\text{H}_2) = 5 \times 10^4 \text{ cm}^{-3}$  and decreases to  $A_V^{\text{tr}} \sim 2.5$  for  $n(\text{H}_2) = 2 \times 10^4 \text{ cm}^{-3}$  (see Figure 6). Interestingly, the very steep slope begins from  $A_V^{\text{tr}}$  where grain alignment has not yet decreased significantly, i.e., the lines of sight  $A_V \sim A_V^{\text{tr}}$  still go through the region with  $a_{\text{ali}} \ll a_{\text{max}}$  (see Figure 5 for model 3).

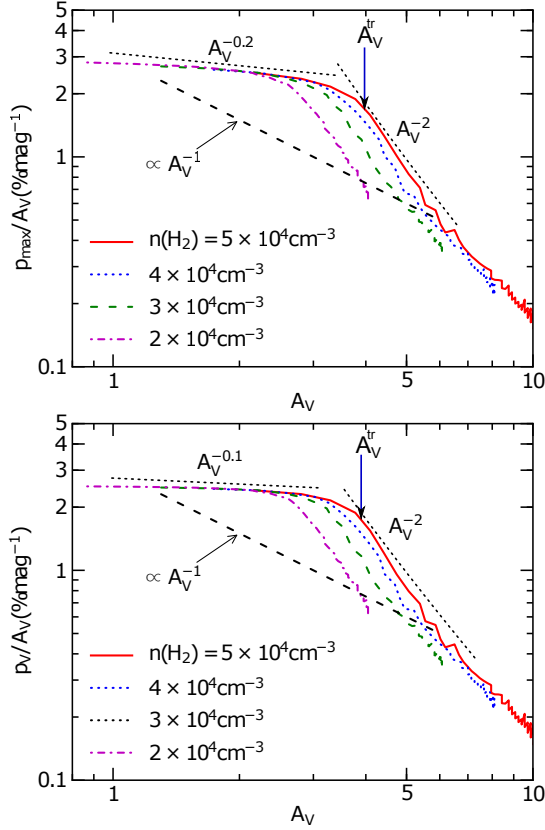
5.1.2 *Three-dimensional case*

Due to its spherical symmetry, the three-dimensional cloud is equivalent to consisting of  $N_y$  circular slabs superimposed with the slab radius decreasing with increasing  $|y| = 0$ . With the assumption of parallel radiation beams from  $\gamma$  Cas and uniform gas density, calculations for  $a_{\text{ali}}$  and polarization  $p_\lambda$  for the three-dimensional cloud can be obtained using the results from the two-dimensional case.

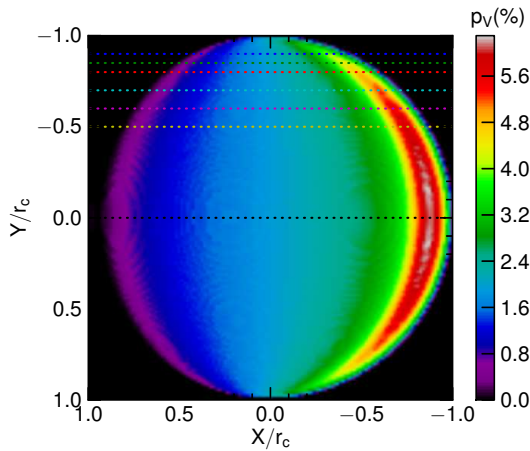
To this end, in the two-dimensional case, we have also created data tables of  $a_{\text{ali}}(x, y = 0, z)$  and  $dp_\lambda(x, y = 0, z)$  calculated by Equation (32) using  $a_{\text{ali}}(x, z)$ . Then, we interpolate for  $dp_\lambda(x, y, z)$  for a cell at  $y$  coordinate using the dependence of  $dp_\lambda(x, y = 0, z)$  on  $\tau_x(x, y = 0, z)$  with regard to  $\gamma$  Cas. For example, for a given coordinate  $z$  in the cloud, we have a  $xy$  grid. Since  $\tau_x(x, y = 0, z)$  is already calculated, one can easily calculate  $\tau_x(x, y, z)$  for each cell  $(x, y)$  of thickness  $dz$ . Then,  $dp_\lambda(x, y, z)$  is obtained by interpolating  $dp_\lambda(x, y = 0, z)$  as a function of  $\tau_x(x, y = 0, z)$  for a given  $\tau_x(x, y, z)$ . Finally, we interpolate for  $dp_\lambda(X, Y, Z)$  using  $dp_\lambda(x, y, z)$  and the coordinate transformation from  $\hat{x}\hat{y}\hat{z}$  to  $\hat{X}\hat{Y}\hat{Z}$ . Polarization in the POS,  $p_\lambda(X, Y)$ , is obtained by integrating  $dp_\lambda(X, Y, Z)$  along the  $\hat{Z}$  axis.

Figure 7 shows the map of  $p_V(X, Y)$  in the POS. As expected from the maps of grain alignment (Figure 4), the polarization is stronger in the dayside of the cloud and decreases significantly toward the nightside. The polarization appears to peak in the region very close to the cloud surface (red), extending from  $Y/r_c = -0.6$  to  $+0.6$ . On the nightside of IC 63, the stellar radiation is significantly reduced due to dust extinction and the fraction of aligned grains decreases, which results in the substantial decrease of polarization.

Figure 8 shows our model predictions for  $p_V/A_V$  (upper) and  $\lambda_{\text{max}}$  (lower) across the entire surface of IC 63. Results for background stars behind the dayside (orange circles) exhibit higher  $p_V/A_V$  and lower  $\lambda_{\text{max}}$  that the stars behind the nightside (blue



**Figure 6.** Variation of fractional polarization  $p/A_V$  as a function of  $A_V$  for four models of IC 63 (see the text). The left and right panels show  $p_{\max}/A_V$  and  $p_V/A_V$ , respectively. Two-stage variation of  $p/A_V$  vs.  $A_V$  is observed with a shallow slope for  $A_V < 3$  and steep slope for  $A_V > 4$ . Dotted lines show the approximate power laws of  $p/A_V$  vs.  $A_V$ , and arrows mark the transition position with  $A_V^{tr}$ . The dashed line shows  $p/A_V \propto A_V^{-1}$ . Grain alignment by only RATs is considered.



**Figure 7.** Map of  $p_V$  in the POS,  $\hat{X}\hat{Y}$ . Stellar radiation projected onto the POS is parallel to the  $\hat{X}$  axis (from negative to positive  $X$ ). Dotted lines show the different cuts ( $Y/r_c = 0.0, -0.5, -0.6, -0.7, -0.8, -0.85$  and  $-0.9$ ) along  $\hat{X}$ . The polarization in the dayside is stronger than in the nightside due to its stronger radiation intensity. Along a horizontal cut (constant  $Y$ ),  $p_V$  first increases to its maximum and then declines substantially toward the night side.

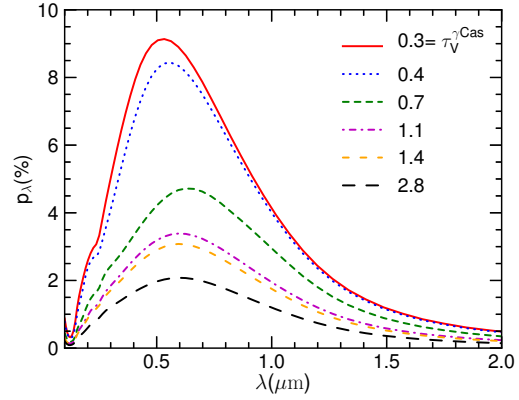


**Figure 10.** Polarization curves for the alignment by both RATs and  $H_2$  torques. The surface density of active site  $\alpha = 10^{12} \text{ cm}^{-2}$  is considered.

circles). A sharp decline of  $p_V/A_V$  at  $A_V \sim 3$  is clearly seen, which is a direct consequence of the loss of grain alignment due to reddening of radiation field (see also Figure 6).

## 5.2 Grain Alignment by both RATs and $H_2$ formation torques

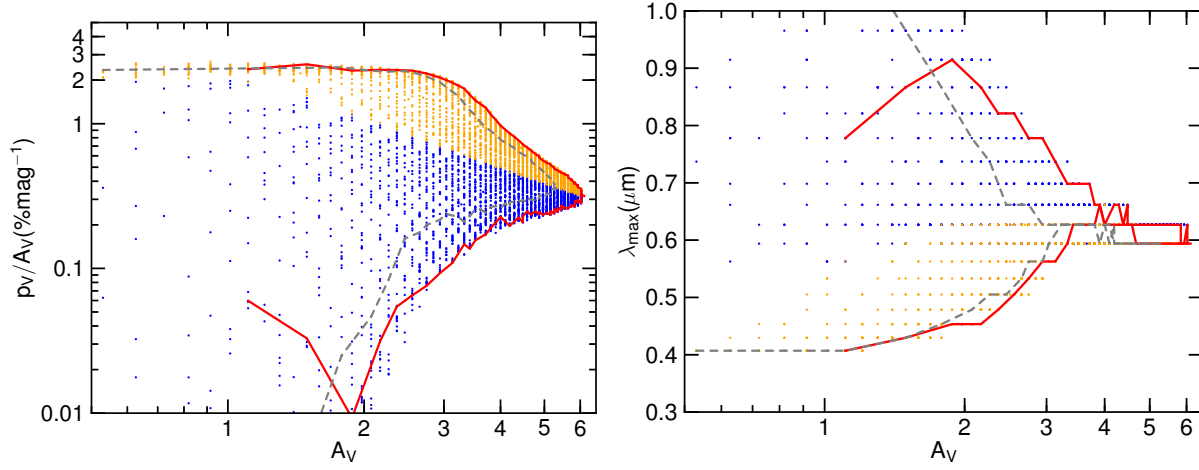
Below, we investigate the effects of  $H_2$  torques on the grain alignment and resulting polarization curves.

The magnitude of  $H_2$  torques is given by Equation (14), which depends on the fraction of atomic hydrogen and the surface density of catalytic site. Calculations in Jansen et al. (1995) for IC 63 show that the fraction of atomic hydrogen decreases rapidly from the surface and becomes negligible ( $\leq 10^{-2}$ ) for  $\tau_V > 1$ . Therefore, for our modeling, we account for  $H_2$  torques for the outer region only, which is characterized by  $\tau_V^{\gamma_{\text{Cas}}} \leq 0.25$  where  $\tau_V^{\gamma_{\text{Cas}}} = 0.25$  corresponds to  $\tau(\lambda = 1100\text{\AA}) = 1$  with  $1110\text{\AA}$  being the cutoff wavelength for  $H_2$  photodissociation. We assume the fraction of atomic hydrogen  $n(\text{H})/n_{\text{H}} = 0.9$  for  $\tau_V^{\gamma_{\text{Cas}}} \leq 0.25$  and  $n(\text{H})/n_{\text{H}} = 0.1$  for  $\tau_V^{\gamma_{\text{Cas}}} > 0.25$ . To study the dependence of grain alignment on the magnitude of  $H_2$  torques, we consider several values of the density of active sites,  $\alpha = 10^{11} \text{ cm}^{-2}, 4 \times 10^{11} \text{ cm}^{-2}, 10^{12} \text{ cm}^{-2}$  and  $10^{13} \text{ cm}^{-2}$ . The rate of thermal flipping and the reduction factor  $\Delta f$  as functions of grain size are taken from Hoang & Lazarian (2009b) (see Section 3.1 and 3.2 for discussion). The results presented here are for model 3, unless specified otherwise.

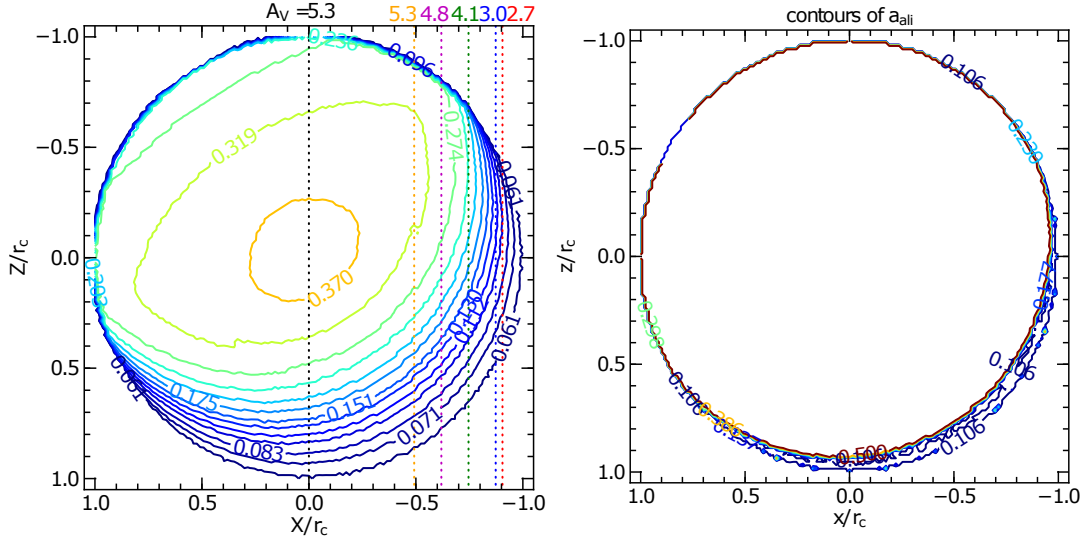
In the left panel of Figure 9 we show the contours of  $a_{\text{ali}}$  in the presence of both RATs and  $H_2$  formation torques. Comparing to Figure 5, we can see that the presence of  $H_2$  torques has a minor effect on  $a_{\text{ali}}$ , which indicates that, for the chosen  $\alpha = 10^{12} \text{ cm}^{-2}$ , the value  $a_{\text{ali}}$  is mainly determined by strong RATs. The effect of  $H_2$  torques in creating the new high- $J$  attractor points is shown in the right panel where grains larger than  $a'_{\text{ali}} \sim 0.1 \mu\text{m}$  become perfectly aligned.

Figure 10 shows the polarization curves for the RAT alignment with  $H_2$  torques included. It can be seen that the polarization increases in the presence of  $H_2$  torques. The effect is most significant for the sightlines with lower  $\tau_V^{\gamma_{\text{Cas}}}$ , which go through a thin layer near the surface. One interesting feature is that  $\lambda_{\text{max}}$  for the sightline  $\tau_V^{\gamma_{\text{Cas}}} = 0.4$  is substantially increased.

Figure 11 (left panel) shows the variation of the fractional polarization with the magnitude of  $H_2$  torques, which is obtained by varying  $\alpha^{-1}$  while other parameters unchanged. As shown,  $p_V/A_V$  tends to increase with the increasing  $\alpha^{-1}$ , i.e., the mag-



**Figure 8.** Variation of  $p_V/A_V$  (left) and  $\lambda_{\max}$  (right) vs.  $A_V$  over the entire IC 63 surface. Each dot corresponds to a line of sight toward background stars. Orange circles denote the lines of sight through the dayside and blue circles denote the lines of sight through the nightside of IC 63. Solid and dashed lines show the variation  $p/A_V$  along the direction  $Y/r_c = 0$  and  $Y/r_c = 0.5$ .



**Figure 9.** Left panel: similar to Figure 5, but for the alignment driven by both RATs and  $H_2$  torques. Right panel: contours of grain size  $a'_{\text{ali}}$  above which grains are perfectly aligned due to effect of  $H_2$  torques. The surface density of active site  $\alpha = 10^{12} \text{ cm}^{-2}$  is considered.

nitude of  $H_2$  torques when the  $H_2$  torques are sufficiently strong (i.e.  $\alpha^{-1} > 5 \times 10^{-14} \text{ cm}^2$ ). The effect is most profound for the sightline through the thin surface layer with  $\tau_V^{\gamma \text{Cas}} < 0.5$ .

The variation of the peak wavelength  $\lambda_{\max}$  with  $\alpha^{-1}$  is shown in the right panel of Figure 11. It shows that  $\lambda_{\max}$  does not increase monotonically with  $\alpha^{-1}$ . For sightlines with  $\tau_V^{\gamma \text{Cas}} < 0.5$ ,  $\lambda_{\max}$  increases with increasing  $\alpha^{-1}$  initially, then it falls when  $\alpha^{-1}$  becomes sufficiently large at  $\alpha^{-1} \sim 10^{13} \text{ cm}^2$ . Such a variation can be explained as the followings. Due to strong RATs near the surface, even small grains can be radiatively aligned. For these small grains, the thermal flipping significantly suppresses the effect of  $H_2$  torques acting at their high- $J$  attractor points, such that  $H_2$  torques have minor effects on  $a_{\text{ali}}$  determined by RATs. However, at low- $J$  attractor points,  $H_2$  torques can drive some intermediate ( $a > a'_{\text{ali}}$ ) grains to suprathermal rotation, increasing the degree of alignment of intermediate and large grains. As a result, the contribution of aligned, large grains to the total polarization increases, resulting in larger  $\lambda_{\max}$ . When  $H_2$  torques become very strong (rather high

$\alpha^{-1}$ ), the range of perfect alignment becomes broader due to the decrease of  $a'_{\text{ali}}$  (the upper dashed line in Figure 1 extends to rather small grains). As a result,  $\lambda_{\max}$  is shifted to the blue. For the range of  $\alpha$  considered and  $\tau_V^{\gamma \text{Cas}} < 0.3$ ,  $\lambda_{\max}$  is in general larger than that in the case without (or low)  $H_2$  torques (see right panel).

### 5.3 Comparison of model predictions with observations and evidence of $H_2$ torques

Figure 12 shows the maps of  $p_V/A_V$  predicted for grain alignment by RATs (upper panels) and by both RATs and  $H_2$  torques (lower panels). Model 4 (left panels) and 3 (right panels) of IC 63 are shown. The presence of  $H_2$  torques results in the increase of  $p_V/A_V$  in a thin layer close to  $\gamma$  Cas (red region). Model with lower density appears to have larger  $p/A_V$  at the same distance from  $\gamma$  Cas (X value to the right).

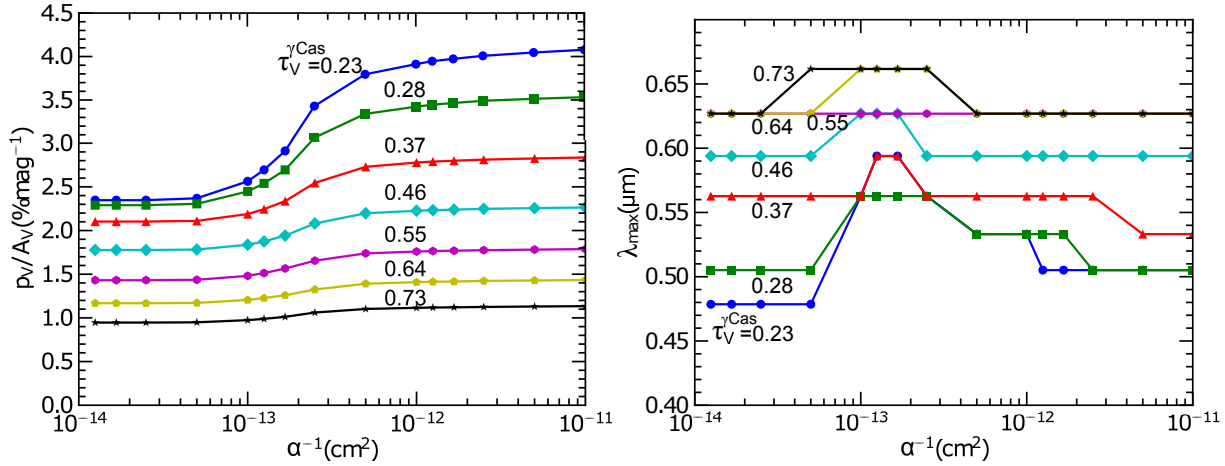


**Figure 11.** Variation of  $p_V/A_V$  (left) and  $\lambda_{\max}$  (right) with the magnitude of  $H_2$  torques ( $\alpha^{-1}$ ) for different sightlines with  $\tau_V^{\gamma\text{Cas}}$  indicated.  $p_V/A_V$  begins to increase with  $\alpha^{-1}$  for  $\alpha^{-1} > 5 \times 10^{-14} \text{ cm}^2$ . The middle slab ( $Y/r_c = 0$ ) is considered.

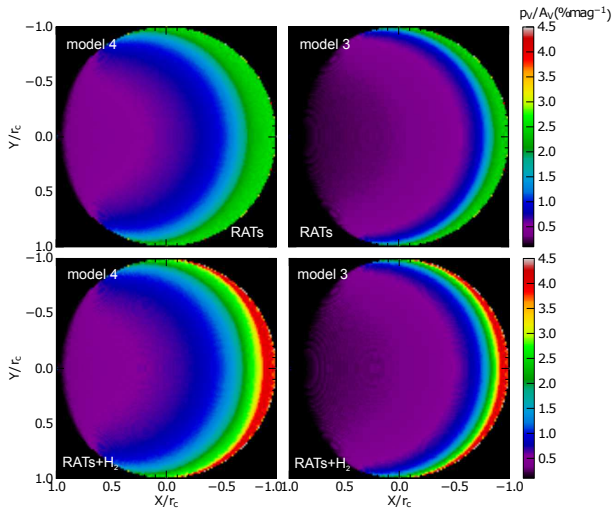


**Figure 12.** Fractional polarization  $p_V/A_V$  in the POS for the grain alignment by RATs without (upper) and with (lower)  $H_2$  torques. The fractional polarization is strongest near the cloud surface facing  $\gamma$  Cas. The presence of  $H_2$  torques increases significantly the fractional polarization in the thin layers (red regions) of the dayside surface.

To facilitate comparison between predicted results and observational data, in Figure 13, we illustrate the projections of stars on to the POS and the spherical cloud of radius  $r_c$  (red circle) which encloses the compression ridge adopted for our modeling. This spherical cloud encompasses most of the projections of stars whereas the projections of stars #8, #11 and #52 appear to belong to a nearby cloud (yellow circle).

In Figure 14 we plot  $p_V/A_V$  versus  $A_V$  obtained from modeling (circle symbols) against the observational data (square symbols) from Andersson et al. (2013). Here model 3 is considered. Stars #5, #8 and #11 (red squares) exhibit strong  $H_2$  formation, and the remaining stars (blue squares) do not.<sup>3</sup>

<sup>3</sup> It is worthy noting that for star #5, with indication of high  $H_2$  formation rate, the  $A_V$  value is uncertain. The observationally derived value of the total-to-selective extinction ( $R_V$ ) for this star is very large relative to the rest of the sample. Andersson et al. (2013) argued that this might be due

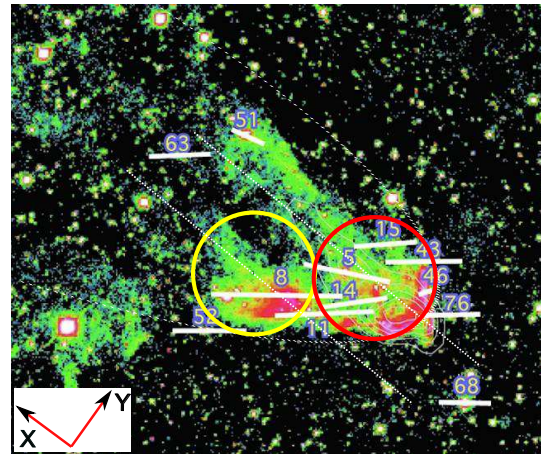


**Figure 13.** Projections of stars on to the POS with their observed V-band polarization vectors (white bars) are indicated. Image shows emission intensity through a narrow-band filter centered on the  $H_2$  1–0 S(1) line at  $2.122 \mu\text{m}$  for IC 63. Red circle encompasses the nose that is modeled by a spherical cloud of radius  $r_c = 0.03 \text{ pc}$  or  $31''$  for the distance of  $\gamma$  Cas  $D = 200 \text{ pc}$ . Background stars 8 and 11 and 52 in the POS are assumed to lie in another circle of the same radius. Dotted lines are parallel to the radiation direction and go through the center of circles. Adapted from (Andersson et al. 2013).

Figure 14 (left panel) indicates that the RAT alignment can successfully reproduce the observational data for the stars with low  $H_2$  formation. However, the alignment by only RATs cannot reproduce the highest values  $p_V/A_V$  for the three stars (#5, #8, #11) having strong  $H_2$  formation. In the presence of  $H_2$  torques, the right panel shows that our model can successfully reproduce the highest  $p_V/A_V$  of these stars. *Is this a potential evidence for the enhancement of alignment by  $H_2$  torques?* The answer is probably yes.

From the left panel, it is apparent that the model of RAT

either to that this sightline contains unusually large grains, in which case the estimated value of  $A_V = 4.06$  (marked with purple) is appropriate. If, on the other hand, the large  $R_V$  is due to, e.g., a unresolved red companion (i.e. a systematic photometric error), calculating  $A_V$  with an  $R_V$  value based on the average of the remaining background stars would yield  $A_V = 1.18$ .

alignment would reproduce the highest observed level if  $p_V/A_V$  is increased by a factor  $\sim 1.5$ . This can be fulfilled by increasing the fraction of grains aligned with high- $J$  attractor points from  $f_{\text{high}J} = 0.5$  to  $f_{\text{high}J} \sim 0.75$  (i.e., most of grains are perfectly aligned at high- $J$  attractor points). Based on theoretical considerations, such a high value  $f_{\text{high}J}$  seems less likely for the RAT alignment of normal paramagnetic dust and typical magnetic field strengths. Therefore, the effect of  $\text{H}_2$  torques appears to be favored for the cause of enhanced  $p_V/A_V$  observed for the stars with strong  $\text{H}_2$  formation because it does not require a significant fraction of grains aligned at high- $J$  attractor points.

Let us compare the predicted results with the observational data in more detail. First, star #46 has fractional polarization much lower than predicted by our model with  $f_{\text{high}J} = 0.5$  (see Figure 14). This discrepancy indicates that this star has the stronger disalignment than the model assumption (i.e., gas density and temperature). This is supported by  $\text{HCO}^+$  mapping by Polehampton et al. (2005) (see also Andersson et al. 2013).

Second, the model predictions are in good general agreement with the observation for the stars without (or low efficiency)  $\text{H}_2$  formation. Indeed, the polarization of these stars (blue squares) can be reproduced by the model of RAT alignment, although two stars #75 and #76 are slightly above the prediction. Moreover, the photometry image shows that two stars #63 and #68 with low  $p_V/A_V$  are located more distant from  $\gamma$  Cas than the others. The polarization for these stars can be successfully reproduced by our modeling for lines of sight through the middle region (dots in the lower bound).

The polarization of the stars with indication of efficient  $\text{H}_2$  formation (red squares) can be reproduced by the model with  $\text{H}_2$  torques evaluated near the equator ( $Y \sim 0$ , upper bound). The lines of sight toward stars #8 and #11 appear to lie outside the spherical cloud (namely cloud 1) of the nebula that we carried out the modeling (red circle in Figure 13), but they can be considered to be in another spherical cloud (namely cloud 2 (yellow circle in Figure 13)). Assuming that the density of these two clouds are the same and the same radius, then, we expect that the grain alignment in cloud 2 is similar to that in cloud 1 for which these stars could be reproduced by the models for the stars near the surface of cloud 1.

Finally, the model with  $\text{H}_2$  torques can also reproduce the fractional polarization for stars #75 and #76. Thus, these stars may have weaker collisional disalignment or have some alignment enhancement due to  $\text{H}_2$  formation.

Figure 15 shows  $\lambda_{\text{max}}$  vs.  $A_V$  for the case of alignment without (left) and with (right)  $\text{H}_2$  torques. Near the surface (e.g.,  $A_V < 2$ ), the alignment by only RATs has low  $\lambda_{\text{max}}$ , which appears below the observed data (left panel). The inclusion of  $\text{H}_2$  torques results in the increase of  $\lambda_{\text{max}}$  (see also Figure 11, right panel) in this outer layer and produces a better agreement between the predicted  $\lambda_{\text{max}}$  and the observational data (right panel).

The above comparison is based on our model 3, but we expect the main conclusions to remain valid also for model 1,2 and 4, because of the systematic dependence of  $p_V/A_V$  on gas density.

## 6 DISCUSSION

### 6.1 Previous studies on the RAT alignment in dense molecular clouds

Grain alignment by RATs in starless, dense, clouds has been studied by a number of authors (Cho & Lazarian 2005; Bethell et al.

2007; Whittet et al. 2008). These studies dealt with the alignment of grains by RATs induced by the attenuated ISRF. The alignment of grains inside the cloud depends on the radiation intensity determined by the depth (i.e., extinction) from the cloud surface and grain rotational damping (i.e., collisions through the gas density and temperature). Those studies concluded that grains can efficiently be aligned by RATs. Even in the cloud interior with  $A_V \geq 10$ , large grains can still be aligned because the RATs associated with the remaining, reddened light couple to the larger grain sizes. The fractional polarization is observed to decrease with increasing  $A_V$ , which is consistent with the predictions by RAT alignment mechanism.

The simple, one-dimensional modeling of RAT alignment for a starless core in Whittet et al. (2008) shows that the alignment in the dense cloud follows the model in which aligned grains are distributed in the outer layers, and the innermost region contains non-aligned grains. As a result, the fractional polarization is predicted to first decrease slowly with  $A_V$  and then decline more rapidly according to a power law  $A_V^{-1}$  from some large  $A_V \sim 3$ .

### 6.2 RAT alignment in reflection nebula

The present work is the first theoretical study dealing with the alignment of dust grains in a reflection nebula, a dense molecular cloud illuminated by a nearby star as well as the attenuated ISRF. For the conditions of high gas density and temperature of the reflection nebula, we found that the alignment is mainly determined by the strong stellar radiation, while the attenuated ISRF is inefficient in aligning grains, even in the thin layers of the envelope due to efficient collisional randomization.

Our results also reveal that the fractional polarization is strong in the dayside facing the star and rather low in the nightside. In the spirit of RAT alignment, this is straightforward because grains closer to the surface would receive higher stellar radiation intensity, which results in the higher fractional polarization.

Observational studies for grain alignment in molecular clouds usually characterize the fractional polarization  $p_V/A_V$  by a single power law, ranging from the cloud surface to center (e.g., Whittet et al. 2008; Andersson et al. 2013). Based on detailed modeling of RAT alignment, it appears that such a description by a single power law may not reflect the realistic variation of grain alignment in the cloud. For IC 63, our results show that the variation of  $p_V/A_V$  with  $A_V$  in general follows two stages, well characterized by a power law  $p_V/A_V \propto A_V^\eta$  with the different slopes  $\eta$ . In the first stage,  $p_V/A_V$  decreases slowly with  $A_V$  with  $\eta \sim -0.1$ . In the second stage,  $p_V/A_V$  declines steeply with  $\eta \sim -2$  (see Figure 6).

The presence of a very steep slope ( $\eta \sim -2$ ) starting from  $A_V^{\text{tr}}$  is surprising, although a steep slope  $\eta \sim -1.1$  was reported for IC 63 in Andersson et al. (2013). But it seems to be clear by considering the geometry of IC 63 and relative position of stellar source in the context of RAT alignment. Indeed, the alignment of grains inside the spherical reflection nebula is mainly produced by stellar radiation, which depends on the relative position of  $\gamma$  Cas and IC 63. Grains in the dayside are directly illuminated by stellar radiation and can be aligned efficiently, whereas grains in the nightside receive much less radiation and are weakly aligned. The outer layers containing aligned grains have a thickness that decreases with increasing distance from the star, corresponding to an increasing  $A_V$  (see Figure 4). Since the polarization of starlight is proportional to the column density of aligned grains along the sightline, the decrease in thickness of the layer with aligned grains results

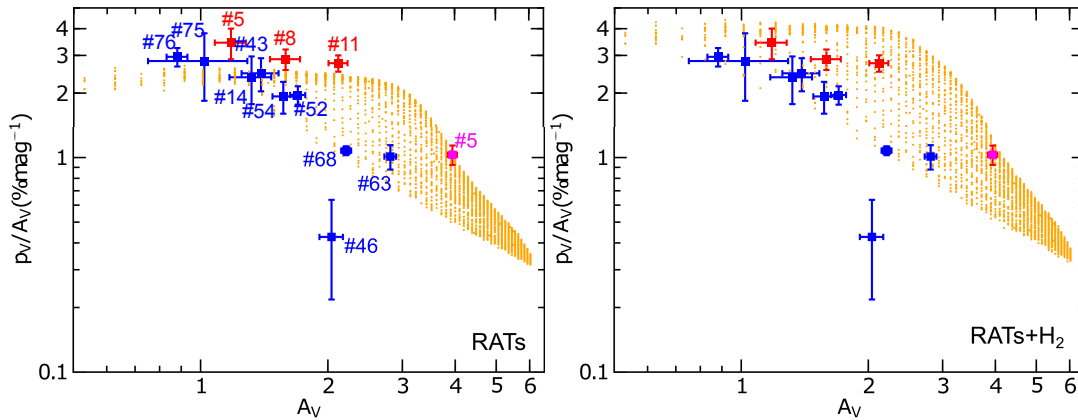


**Figure 14.** Fractional polarization  $p_V/A_V$  vs.  $A_V$  from modeling (circle symbols) compared with the observational data (filled square symbols) for the cases without (left) and with  $H_2$  torques (right). Each circle corresponds to a line of sight through IC 63. The observed stars with high  $p_V/A_V$  are shown in red and other stars with lower  $p_V/A_V$  are shown in blue. Red and purple colors for star #5 indicate two possible  $A_V$  estimated for this star. Predictions for background stars behind the dayside of IC 63 ( $X < 0$ ) (dayside) are shown (see Figure 12).

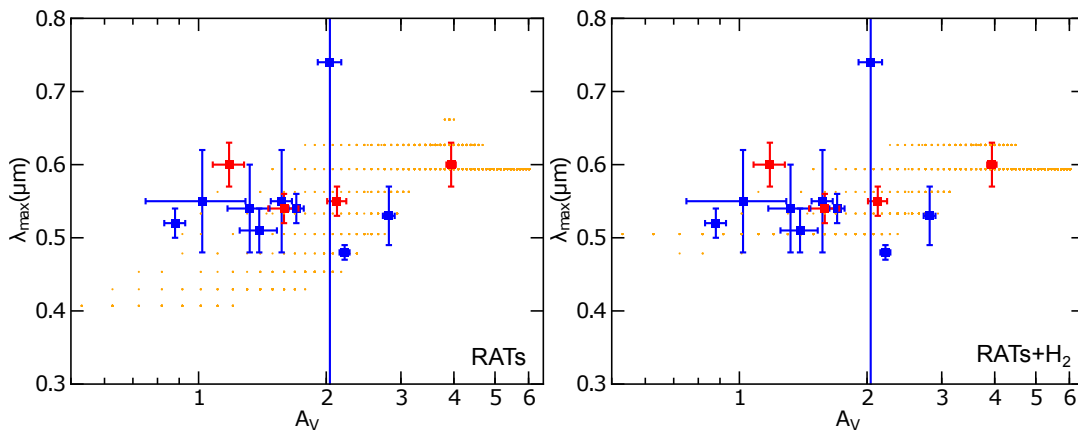


**Figure 15.** Peak wavelength  $\lambda_{\max}$  as a function of  $A_V$ . Left panel: predicted  $\lambda_{\max}$  for RAT alignment from the dayside (blue diamonds) are below the observational data for  $A_V < 2$ . Right panel: results with  $H_2$  torques included, model predictions of  $\lambda_{\max}$  become better agreement with observations.

in the decrease of the polarization (see 4, lower panel). As a result, the fractional polarization declines steeper than  $1/A_V$  predicted for models of RAT alignment with diffuse illumination for which the cloud grain alignment is isotropic with respect to the cloud center.

The transition visual extinction  $A_V^{\dagger}$  between the shallow and very steep slopes can provide useful information on to what extent in the cloud the RAT alignment is still significant. We believe that the variation of  $p/A_V$  versus  $A_V$  following the different slopes is a generic feature of RAT alignment in clouds without embedded stars and illuminated by nearby stars. Further observations for grain alignment in reflection nebulae would be useful to consolidate the RAT alignment theory.

It is important to note that the observed fractional polarization will also be affected by the topology and turbulence of the magnetic field along the sightline (Jones et al. 1992), which is expected to result in a slope steeper than  $\eta \sim -0.2$  for moderate  $A_V$  predicted by us for uniform magnetic fields.

### 6.3 Evidence for alignment enhancement by $H_2$ torques

Andersson et al. (2013) found a potential correlation between the polarization stars behind IC 63 and the intensity of  $H_2$  fluorescence  $I(H_2)$  from IC 63, while based on a relatively small number of

points. They suggested that this correlation provides evidence for enhanced alignment of grains by  $H_2$  torques. Based on our detailed modeling for grain alignment in a uniform spherical cloud, simulating IC 63, we find that the fractional polarization  $p_V/A_V$  tends to increase with the increasing the magnitude of  $H_2$  torques, and that it is highest in the thin surface layer facing  $\gamma$  Cas where  $H_2$  formation takes place. Moreover, we find that the highest  $p_V/A_V$  of the stars with indication of strong  $H_2$  formation can successfully be reproduced when  $H_2$  torques are incorporated within the RAT alignment paradigm.

We also showed that the model by RAT alignment cannot reproduce the highest  $p_V/A_V$  observed when 50 percent of grains aligned with high- $J$  attractor points (i.e.,  $f_{\text{high}J} = 0.5$ ). This problem can be resolved by increasing  $f_{\text{high}J}$  by a factor of 1.5, i.e., from  $f_{\text{high}J} = 0.5$  to  $f_{\text{high}J} \sim 0.75$ . However, such a value  $f_{\text{high}J} = 0.75$  perhaps is too high for the alignment by only RATs under typical conditions of the ISM.

We find that the joint action of  $H_2$  torques and RATs can successfully reproduce the observed highest  $p_V/A_V$  with a more reasonable value  $f_{\text{high}J} = 0.5$ . It is noted that the increase  $f_{\text{high}J}$  to unity can be met by the inclusion of superparamagnetic material (iron clusters) into the grain. However, if this is true, then we do not

expect the increase of the polarization degree with the fluorescent emission intensity as observed in [Andersson et al. \(2013\)](#).

The variation of the peak wavelengths  $\lambda_{\max}$  in the presence of  $H_2$  torques appears to support the idea of alignment enhancement due to  $H_2$  torques. Observational data reveals that the averaged peak wavelength in the case of strong  $H_2$  formation is slightly larger than in the case without  $H_2$  formation ([Andersson et al. 2013](#)). Strong  $H_2$  torques are found to have little effect on the alignment of small grains  $a_{\text{ali}}$  due to rapid flipping but can increase  $f_{\text{highJ}}$  of large grains to unity (see Figure 9). As a result, the peak polarization tends to shift to the red (see the right panel of Figure 11), and the predicted  $\lambda_{\max}$  becomes in better agreement with observed ones (see the right panel of Figure 15).

#### 6.4 Constraints on physical parameters of $H_2$ formation

Our modeling predicts the increase of the fractional polarization  $p_V/A_V$  with the increasing magnitude of  $H_2$  torques characterized by  $\alpha^{-1}$  (see Figure 11). Interestingly, the observational data from [Andersson et al. \(2013\)](#) reveal some correlation between  $p_V/A_V$  versus the intensity of  $H_2$  fluorescence,  $I(H_2)$ . Using this correlation, it may be possible to constrain the value  $\alpha$  assuming a constant  $H_2$  formation efficiency  $\gamma_H$  or vice versa.

Based on observational data in (see [Andersson et al. 2013](#)), we estimate the averaged ratio of  $p_V/A_V$  for stars with high  $H_2$  fluorescence to that of stars with zero  $H_2$  fluorescence is  $1.8 \pm 0.4$ . For the low  $H_2$  fluorescence, the averaged ratio is  $1.1 \pm 0.1$ . From Figure 11 we see that the cases  $\alpha^{-1} < 5 \times 10^{-14} \text{ cm}^2$  has a negligible effect on  $p_V/A_V$  as well as  $\lambda_{\max}$ . Thus, the case  $\alpha^{-1} = 10^{-14} \text{ cm}^2$  can be considered as the case of without  $H_2$  fluorescence. Therefore, the value  $\alpha$  required to produce high  $H_2$  fluorescence can be estimated as the following:

$$\frac{p_{AV}(\text{high } \alpha^{-1})}{p_{AV}(\text{low } \alpha^{-1})} = \frac{p_{AV}(\text{high } I_{H_2})}{p_{AV}(\text{zero } I_{H_2})} = 1.8, \quad (33)$$

where  $p_{AV} = p_V/A_V$ .

Using the sightline near the surface with  $\tau_V^{\text{Cas}} = 0.23$  from Figure 11, one obtains

$$p_{AV}(\alpha^{-1}) = 1.8 \times p_{AV}(\alpha^{-1} = 10^{-14} \text{ cm}^2) \approx 4.2, \quad (34)$$

which requires  $\alpha^{-1} \sim 10^{-11} \text{ cm}^2$ .

For the case of low  $H_2$  fluorescence, we get

$$p_{AV}(\alpha^{-1}) = 1.1 \times p_{AV}(\alpha^{-1} = 10^{-14} \text{ cm}^2) \approx 2.6, \quad (35)$$

which corresponds to  $\alpha^{-1} \sim 10^{-13} \text{ cm}^2$ .

As a result, the value  $\alpha^{-1}$  is constrained in the range  $10^{-11} \text{ cm}^2 > \alpha^{-1} > 10^{-14} \text{ cm}^2$  or  $10^{14} \text{ cm}^{-2} > \alpha > 10^{11} \text{ cm}^{-2}$  assuming  $\gamma_H = 0.1$ .

Since the magnitude of  $H_2$  torques is a function of  $\gamma_H \alpha^{-1/2}$  (see Equation 13). The value  $\alpha$  would decrease if  $\gamma_H$  decreases. If we take the minimum  $\alpha$  (strongest  $H_2$  torque) corresponding to one active site per grain, then, we can also constrain the lower limit of  $\gamma_H$ . For instance, for the  $a = 0.1 \mu\text{m}$  grain, we obtain  $\alpha_{\min} \sim 10^9 \text{ cm}^{-2}$ , which yields  $\gamma_H > 0.1 \times (10^{11}/10^9)^{-1/2} > 0.01$ .

#### 6.5 Recent observational studies of dust polarization

Planck polarization data over the entire sky ([Planck Collaboration et al. 2014b](#)) shows a general decrease of the fractional polarization with gas column density  $N_H$ . From their figure 18, we see that the variation of the mean polarization can be approximately described by a shallow slope with

$\eta \sim -0.2$  and a steep slope  $\eta = -1$  for  $N_H \geq 2 \times 10^{22} \text{ cm}^{-2}$  (i.e.,  $A_V > 10$ ), respectively. Our modeling of RAT alignment, although for a specific nebula (see Figure 8), seems to well reproduce the shallow slope observed. Moreover, the steep slope  $\eta = -1$  for high  $A_V$  seen by *Planck* is expected from the RAT alignment theory that predicts a significant loss of grain alignment toward the center of clouds.

[Jones et al. \(2014\)](#) study the variation of  $p_K/\tau_K$  vs.  $A_V$  for starless cores with  $A_V$  up to 100, which exhibits a shallow and steep slope. For  $A_V < 10$ , their data exhibit a typical slope  $\eta \sim -0.5$ , and a transition to the steep slope at  $A_V \sim 10$  indicates a significant loss of grain alignment as pointed out in [Whittet et al. \(2008\)](#). Accounting for the decrease of grain alignment toward high  $A_V$  as predicted by RAT alignment in their JDK model ([Jones et al. 1992](#)), Jones et al. successfully fit their data with a power law  $p_K/\tau_K \propto A_V^{-1}$  for  $A_V > 10$ .

[Alves et al. \(2014\)](#) investigate the variation of  $p/A_V$  for the starless Pipe nebula using optical, near-infrared (NIR), and submillimeter polarimetry. Interestingly, their NIR data show a steep slope  $\eta \sim -1$  for  $A_V < 9.5$  and a shallow slope  $\eta \sim -0.34$  for  $A_V \sim 9.5 - 30$ . The steep slope is consistent with the prediction of RAT alignment. The interesting shallow slope at higher  $A_V$  may originate from grain growth that occurs in very dense regions of the cloud, which results in additional alignment of big grains and produce a shallower slope as expected from the RAT alignment theory. On the other hand, it may arise from magnetic field turbulence. [Jones et al. \(1992\)](#) show that for a magnetic field structure with a fixed "average" magnetic field and a strong random component, when you transverse a few "unit cells" (lower  $A_V$ ), a slope of  $\eta \sim -0.5$  is expected from a random walk effect. When the number of "cells" approaches infinity, the slope becomes shallower, because while the random field averages away, "eventually" the "constant" field shows back up again.

[Andersson et al. \(2015\)](#) observe a clear break from a shallow slope  $p/A_V \propto A_V^{-0.6}$  to steep slope  $p/A_V \propto A_V^{-1.0}$  at  $A_V \sim 20$  in the starless core L 183. The observational results indicate that the variation of the fractional polarization in molecular clouds is complicated and can be described by a power law with the shallow and steep slopes. The RAT alignment naturally predicts such a variation of  $p/A_V$ .

#### 6.6 Final notes

Grain alignment stayed for decades as a mystery, which impeded the efforts to use dust polarization by aligned grains for studying magnetic fields. Shortly from the beginning of the research, the Davis-Greenstein alignment was identified as the major alignment process in spite of the problems with quantitative accounting for the observational data. The situation has been changed rather recently when RATs became a predictive theory. A big advantage of AMO is that it provides an analytical description of RATs that can account for the fundamental properties of RATs and the form of the torques is simple enough that the effect of several physical processes in addition to RATs is possible to study. This has opened avenues for modeling of the RAT alignment.

This paper is an attempt to provide the modeling of the effects of  $H_2$  torques for a particular astrophysical object in order to directly compare the theoretical predictions with observations. Lastly, with our aim to devise a RAT alignment model that captures fundamental properties of RAT alignment theory, our model does not consider explicitly the effects of the decrease of polarization



due to turbulence (see Cho & Lazarian 2005; Bethell et al. 2007). This issue will be addressed in our future paper.

## 7 SUMMARY

We have carried out a detailed modeling of grain alignment and dust polarization for a reflection nebula using RAT alignment theory. The specific model includes a high, anisotropic, radiation intensity impinging on a cloud with a temperature characteristic of the diffuse ISM but a gas density typical of a molecular cloud. As such, the collisional damping rate of the grain alignment is expected to be significantly higher than in the diffuse ISM, which is also borne out by our modeling. Our principal results can be summarized as follows:

1. Grains are efficiently aligned by RATs in the outer layers of the dayside close to the star, whereas the alignment becomes less efficient in the nightside of the nebula due to the extinction of stellar radiation. In an ideal spherical cloud, the fractional polarization in the dayside facing the star is higher than in the nightside.

2. For a middle slab in the direction of the stellar radiation, the fractional polarization  $p_V/A_V$  slowly decreases with increasing  $A_V$  (i.e., more distant from  $\gamma$  Cas) and then rapidly declines from some transition value of  $A_V$  to  $A_V^{\max}$  due to the gradual loss of aligned grains in the cloud interior. The variation of  $p_V/A_V$  with  $A_V$  can be described by a power law  $A_V^\eta$  with the slope  $\eta = -0.1$  ( $-0.2$ ) for the shallow stage and  $\eta \sim -2$  for the very steep stage.

3. Our predictions for  $p_V/A_V$  and peak wavelength  $\lambda_{\max}$ , based on the RAT alignment, are essentially consistent with the observational data. We show that the stars observed with lower fractional polarization (stars without indication of  $H_2$  formation activity) can be successfully reproduced by our model of alignment by RATs only.

4. We find the increase of the polarization fraction with the increasing magnitude of  $H_2$  formation torques. Applying to IC 63, we show that the inclusion of  $H_2$  formation torques in the model of RAT alignment can successfully reproduce the highest fractional polarization observed for stars with indication of strong  $H_2$  formation. The agreement between the predicted and observed  $\lambda_{\max}$  is significantly improved. These results provide valuable evidence in favor of a role for  $H_2$  torques in grain alignment.

5. Physical parameters related to  $H_2$  formation, including the density of active site and  $H_2$  formation efficiency, may be constrained using the observed fractional polarization and the model prediction. Additional data and more detailed three-dimensional modeling will allow this effect to be more definitely probed using our theoretical tools.

## ACKNOWLEDGMENTS

We thank the referee for her/his insightful and valuable comments that improved our paper. A.L. acknowledge the financial support of the NSF grant AST-1109295, Vilas Award and the Center for Magnetic Self-Organization. B-G A. acknowledge financial support from the NSF through grant AST-1109469. T.H. was supported by Humboldt Fellowship at Ruhr-Universität Bochum.

## APPENDIX A: ANGLE DEPENDENCE OF MAXIMUM ANGULAR MOMENTUM SPUN-UP BY RATs

Here we provide a more intuitive derivation for Equation 23 than in Hoang & Lazarian (2014).

Following AMO, the components of RAT efficiency after averaging over fast grain rotation reads (Equations (61) and (62) in LH07)

$$Q_{e1}(\Theta) = Q_{e1}^{\max} (5 \cos^2 \Theta - 2) / 3, \quad (\text{A1})$$

$$Q_{e2}(\Theta) = Q_{e2}^{\max} \sin(2\Theta), \quad (\text{A2})$$

where  $\Theta$  denotes the angle between  $\hat{\mathbf{a}}_1$  and  $\mathbf{k}$ , and  $Q_{ei}^{\max}$  is the maximum value of RAT component  $Q_{ei}$ . The  $Q^{\max}$ -ratio is simply defined as  $q^{\max} = Q_{e2}^{\max}/Q_{e1}^{\max}$ .

For the perfect coupling of  $\hat{\mathbf{a}}_1$  with  $\mathbf{J}$  (perfect internal alignment), the RAT efficiency component parallel to  $\mathbf{J}$  which acts to spin-up grains is defined as

$$H = Q_{e1}(\Theta) \cos \Theta + Q_{e2}(\Theta) \sin \Theta, \quad (\text{A3})$$

and the projection of  $\mathbf{I}$  on to  $\mathbf{J}$  is  $\Gamma_J \propto H$ .

Let consider an ambient magnetic fields that makes an angle  $\psi$  with  $\mathbf{k}$  and the perfect alignment of  $\hat{\mathbf{a}}_1$ ,  $\mathbf{J}$  with  $\mathbf{B}$ . For this case,  $\Theta \sim \psi$ , and Equation (A3) becomes

$$H = (Q_{e1}(\psi) \cos \psi + Q_{e2}(\psi) \sin \psi) \quad (\text{A4})$$

Plugging  $Q_{e1}$  and  $Q_{e2}$  into the above equation, we obtain

$$H = \left[ \frac{(5 \cos^2 \psi - 2) q^{\max}}{3} + 2 \sin^2 \psi \right] Q_{e2}^{\max} \cos \psi. \quad (\text{A5})$$

The default model of AMO in which the inclination angle of the mirror is 45 degree has  $q^{\max} = 1.2$  (see LH07). With this default  $q^{\max}$  value, the term in the bracket of Equation (A5) becomes independent on  $\psi$ , and can be rewritten as

$$H = Q_{e1}(\psi = 0) \cos \psi. \quad (\text{A6})$$

Since  $\Gamma_J(\psi) \propto H = Q_{e1}(\psi = 0) \cos \psi$ , following Equation (11) we can write

$$J_{\max}^{\text{RAT}}(\psi) = J_{\max}^{\text{RAT}}(\psi = 0) \cos \psi. \quad (\text{A7})$$

## APPENDIX B: DERIVATION OF LONG-LIVED $H_2$ TORQUES

Torques produced by hydrogen formations are studied by numerous authors. Here, we provide the main results for reference.

Let us consider a right square prism of width  $2a_2$  and height  $2a_1$  and  $r = a_2/2a_1$ . The total surface area is  $S = 8r(r + 1)(2a_1)^2$ . Let  $\alpha$  be the density of active sites on the grain surface, thus, the total number of active sites is  $\nu = \alpha S = \alpha 8r(r + 1)(2a_1)^2$ . Note that each site has a radius of about 10 Angstrom, so numerous H atoms can be stuck and form simultaneously hydrogen molecules. Since each site has small area, the temperature of the site can be uniform, such that H molecules evaporate from the site can have the same mean kinetic energy but different direction. The torque induced by evaporating molecules from each active site can be calculated as follows.

Consider a surface perpendicular to  $\hat{\mathbf{a}}_1$  axis, the collision rate of H atoms from gas of density  $dn(\mathbf{v})$  with velocity  $\mathbf{v}$  in  $\mathbf{v}$ ,  $\mathbf{v} + d\mathbf{v}$  is given by

$$dR_{\text{coll}} = dn(\mathbf{v})v_z dA, \quad (\text{B1})$$

where  $v_z > 0$  is the component of velocity parallel to  $\hat{\mathbf{a}}_1$  along which the gas atoms collide with the grain surface,  $dA$  is the surface element with the normal vector along  $\hat{\mathbf{a}}_1$ , and

$$dn(\mathbf{v}) = n_{\text{H}} Z \exp(-\alpha v^2) dv_x dv_y dv_z, \quad (\text{B2})$$

where  $\alpha = m_{\text{H}}/2k_{\text{B}}T_{\text{gas}}$  and  $Z = (\pi/\alpha)^{-3/2}$  is the normalization coefficient.

Integrating over the surface area and over isotropic distribution of gas atom velocity, we obtain

$$R_{\text{coll}} = A_1 \int v_z n_{\text{H}} Z \exp(-\alpha v^2) dv_x dv_y dv_z, \quad (\text{B3})$$

$$= A_1 n_{\text{H}} (\pi/\alpha)^{-3/2} (\pi/\alpha) \int_0^\infty v_z \exp(-\alpha v_z^2) dv_z \quad (\text{B4})$$

$$= A_1 n_{\text{H}} (\pi/\alpha)^{-1/2} (1/2\alpha) = A_1 n_{\text{H}} \frac{1}{2} \left( \frac{2k_{\text{B}}T_{\text{gas}}}{\pi m_{\text{H}}} \right)^{1/2} \quad (\text{B5})$$

$$= A_1 n_{\text{H}} \frac{\langle v_{\text{H}} \rangle}{4}, \quad (\text{B6})$$

where  $A_1$  is the surface area of the side  $\hat{\mathbf{a}}_1$ , and  $\langle v_{\text{H}} \rangle = (8k_{\text{B}}T_{\text{gas}}/\pi m_{\text{H}})^{1/2}$  is the mean speed of gas atoms. Thus, the collision rate by gas atoms to any surface is equal to the surface area multiplied by the mean flux of incident atoms divided by four.

Due to its isotropic distribution of gas atoms, the total rate of H atoms arriving at the entire grain surface is given by

$$\dot{N}_{\text{H}} = S n_{\text{H}} \frac{\langle v_{\text{H}} \rangle}{4} = n_{\text{H}} \langle v_{\text{H}} \rangle 2r(r+1)(2a_1)^2, \quad (\text{B7})$$

Let  $\gamma_{\text{H}}$  be the fraction of arrival H atoms that form  $\text{H}_2$  molecules, then, the total number of  $\text{H}_2$  can be formed over the entire grain surface is

$$\dot{N}_{\text{mol}} = \frac{\gamma_{\text{H}}}{2} \dot{N}_{\text{H}} = \gamma_{\text{H}}(1-y)n_{\text{H}} \langle v_{\text{H}} \rangle r(r+1)(2a_1)^2. \quad (\text{B8})$$

The number of  $\text{H}_2$  molecules formed per site is then  $\dot{N}_1 = \dot{N}_{\text{mol}}/\nu$ . Assuming that the grain is spinning around its symmetry axis, and we want to calculate the increase of grain angular momentum along its symmetry axis per units of time. As a result, only rockets from the sides of the grain can increase the grain angular momentum in the direction parallel to the grain symmetry axis (i.e., spin the grain up). The number of active sites on the sides is

$$N_{\text{side}} = \alpha 4(2a_1) \times (2a_2) = \alpha 8r(2a_1)^2. \quad (\text{B9})$$

Thus, the fraction of sites useful for spin-up is then  $f_{\text{spin-up}} = N_{\text{side}}/\nu = 1/(r+1)$ .

The angular momentum deposited by one  $\text{H}_2$  molecule is equal to

$$\delta L_z = r(2m_{\text{H}})v \sin \theta, \quad (\text{B10})$$

where  $\theta$  is the angle between the ejection direction of  $\text{H}_2$  molecule and the radius vector  $r$ .

Assuming that the active site is narrow and deep below the grain surface, such that all  $\text{H}_2$  molecules from one active site leave the grain in a single direction and at the same speed. The direction and velocity of escaping  $\text{H}_2$  molecules from different active sites is random, and its instantaneous velocities are given by Maxwellian distribution. The total angular momentum deposited to the grain by all  $\text{H}_2$  molecules leaving active site  $i$ :

$$\delta \mathcal{L}_i = \frac{\dot{N}_{\text{mol}}}{\nu} r(2m_{\text{H}})v \sin \beta, \quad (\text{B11})$$

where  $\beta$  is the angle between  $\mathbf{v}$  and  $\mathbf{r}$ . Approximating the brick as a

thin disk, then,  $\beta = \theta$ , the angle between  $\mathbf{v}$  and the grain tangential direction, and  $r \approx a_2$ .

Summing  $\mathcal{L}_i$  over all active sites (summing over all escaping angles  $\beta$ ) results in zero net angular momentum. However, the total increase of squared angular momentum per units of time is not averaged out to zero and takes the following form:

$$\Delta L_z^2 = \sum_{i=1}^{\nu/(r+1)} \delta \mathcal{L}_i^2. \quad (\text{B12})$$

Because the velocity and direction of escaping molecules from the different active sites are random, we can average the above equation as follows:

$$\langle \Delta L_z^2 \rangle = \frac{\nu}{r+1} \langle \delta \mathcal{L}^2 \rangle, \quad (\text{B13})$$

where

$$\langle \delta \mathcal{L}^2 \rangle = \frac{\dot{N}_{\text{mol}}^2}{\nu^2} r^2 (2m_{\text{H}})^2 \int_0^\infty dv Z v^2 e^{-\alpha v^2} v^2 \int_0^\pi d\phi \int_0^\pi d\theta \sin \theta \cos^2 \theta, \quad (\text{B14})$$

where the integration over  $\phi$  is taken from 0 to  $\pi$  only due to the fact that only outward  $\text{H}_2$  molecules contribute to the recoil.

Using the integral  $\int_0^\infty e^{-\alpha v^2} dv = \pi^{1/2}/2\alpha^{-1/2}$  and  $\int_0^\infty v^4 e^{-\alpha v^2} dv = 3\pi^{1/2}/8\alpha^{-5/2}$ , we obtain

$$\langle \delta \mathcal{L}^2 \rangle = \frac{\dot{N}_{\text{mol}}^2}{\nu^2} a_2^2 \frac{2m_{\text{H}} E_{\text{kin}}}{3}, \quad (\text{B15})$$

where  $E_{\text{kin}} = 3k_{\text{B}}T_{\text{gas}}/2$  is the mean kinetic energy of  $\text{H}_2$  molecules.

Thus,

$$\langle \Delta L_z^2 \rangle = \frac{\nu}{r+1} \frac{\dot{N}_{\text{mol}}^2}{\nu^2} a_2^2 \frac{2m_{\text{H}} E_{\text{kin}}}{3}, \quad (\text{B16})$$

Plugging in  $\dot{N}$  and  $a_2 = 2a_1 r$ , we obtain

$$\langle \Delta L_z^2 \rangle = r^4 (r+1) \gamma_{\text{H}}^2 (1-y)^2 n_{\text{H}}^2 \langle v_{\text{H}} \rangle^2 (2a_1)^6 \left( \frac{2m_{\text{H}} E_{\text{kin}}}{3\nu} \right) \quad (\text{B17})$$

The magnitude of torque due to  $\text{H}_2$  formation is denoted as

$$\Gamma_{\text{H}_2} \equiv \langle \Delta L_z^2 \rangle^{1/2}. \quad (\text{B18})$$

## APPENDIX C: EXTINCTION AND POLARIZATION CROSS-SECTION

### C1 Extinction cross-section

Let us consider a spheroid grain with the symmetry axis  $\hat{\mathbf{a}}_1$ . A perfectly polarized electromagnetic wave with the electric field vector  $\mathbf{E}$  propagates along the  $z$ -axis, which is perpendicular to the symmetry axis. Let  $C_{\text{ext}}(\mathbf{E} \perp \mathbf{a})$  and  $C_{\text{ext}}(\mathbf{E} \parallel \mathbf{a})$  be the extinction of the radiation for the cases in which the electric field vector is parallel and perpendicular to the grain symmetry axis, respectively.

For simplification, we denote these extinction cross-section by  $C_{\perp}$  and  $C_{\parallel}$ . For the general case in which  $\mathbf{E}$  makes an angle  $\theta$  with the symmetry axis, the extinction cross-section becomes

$$C_{\text{ext}} = \cos^2 \theta C_{\parallel} + \sin^2 \theta C_{\perp}, \quad (\text{C1})$$

Since the original starlight is unpolarized, one can compute the total extinction cross-section by integrating Eq. (C1) over the isotropic distribution of  $\theta$ , i.e.,  $f_{\text{iso}} d\theta = \sin \theta / 2 d\theta$ . As a result,

$$C_{\text{ext}} = \frac{1}{3} (2C_{\perp} + C_{\parallel}). \quad (\text{C2})$$

Throughout this paper, the polarization cross-section is defined as

$$C_{\text{pol}} = C_{\perp} - C_{\parallel}, \quad (\text{C3})$$

$$C_{\text{pol}} = \frac{1}{2} (C_{\parallel} - C_{\perp}), \quad (\text{C4})$$

for oblate and prolate spheroidal grains, respectively.

## C2 Polarization cross-section

Consider an observation coordinate system, which is defined by the sightline directed along the  $z$ -axis, the projection of the magnetic field on the POS denoted by the  $y$ -axis, and the third axis is perpendicular to the  $yz$  plane, namely  $x$ -axis. Thus,  $\mathbf{B}$  lies in the  $yz$  plane and makes a so-called angle  $\xi$  with the  $y$ -axis.

By transforming the grain coordinate system to the observer coordinate system and taking corresponding weights, we obtain

$$C_x = C_{\perp} - \frac{C_{\text{pol}}}{2} \sin^2 \beta, \quad (\text{C5})$$

$$C_y = C_{\perp} - \frac{C_{\text{pol}}}{2} (2 \cos^2 \beta \cos^2 \xi + \sin^2 \beta \sin^2 \xi), \quad (\text{C6})$$

where the perfect internal alignment of grain axes with the angular momentum has been assumed.

The polarization cross-section then becomes

$$C_x - C_y = C_{\text{pol}} \frac{(3 \cos^2 \beta - 1)}{2} \cos^2 \xi. \quad (\text{C7})$$

Taking the average of  $C_x - C_y$  over the distribution of the alignment angle  $\beta$ , the above equation can be rewritten as

$$C_x - C_y = C_{\text{pol}} \langle Q_J \rangle \cos^2 \xi, \quad (\text{C8})$$

where

$$Q_J = \frac{(3 \cos^2 \beta - 1)}{2} \quad (\text{C9})$$

is the degree of alignment of the grain angular momentum with the ambient magnetic field.

When the internal alignment is not perfect, following the similar procedure, we obtain

$$C_x - C_y = C_{\text{pol}} \langle Q_J Q_X \rangle \cos^2 \xi \equiv C_{\text{pol}} R \cos^2 \xi, \quad (\text{C10})$$

where  $R = \langle Q_J Q_X \rangle$  is the Rayleigh reduction factor.

## APPENDIX D: RADIATIVE TRANSFER FOR POLARIZED RADIATION

In general, polarized light can be described by the Stokes parameters,  $I$ ,  $Q$ ,  $U$ , and  $V$ .

### D1 General Radiative Transfer Equations

Consider the propagation of unpolarized starlight of intensity  $I_0$  through a medium containing aligned grains. Let  $\gamma_x, \gamma_y$  be the opacity in units of  $\text{cm}^{-1}$ , when the electric field is parallel to the  $\hat{x}$  and  $\hat{y}$  directions, and  $\psi$  is the angle between the projected magnetic field on to the POS and the  $\hat{x}$  axis. Opacity is related to the cross-section per column density follows:

$$d\tau_x = \gamma_x dz = \sigma_x n_{\text{gas}} dz, \quad (\text{D1})$$

$$d\tau_y = \gamma_y dz = \sigma_y n_{\text{gas}} dz, \quad (\text{D2})$$

Thus,

$$\gamma_x = \int C_x \frac{dn}{da} da, \quad \gamma_y = \int C_y \frac{dn}{da} da, \quad (\text{D3})$$

where  $dn/da$  is the grain size distribution.

The opacity related to circular polarization are denoted by  $\delta_x$  and  $\delta_y$ . As a result, RT equations can be written as

$$\frac{d \ln I}{dz} = -\frac{\gamma_x + \gamma_y}{2} + \frac{\Delta\gamma}{2} \left[ \frac{Q}{I} \cos 2\psi + \frac{U}{I} \sin 2\psi \right] \quad (\text{D4})$$

$$\frac{d}{dz} \left( \frac{Q}{I} \right) = \frac{\Delta\gamma}{2} \cos 2\psi + \Delta\delta \frac{V}{I} \sin 2\psi - \frac{\Delta\gamma}{2} \left( \frac{Q}{I} \right) \left[ \frac{Q}{I} \cos 2\psi + \frac{U}{I} \sin 2\psi \right], \quad (\text{D5})$$

$$\frac{d}{dz} \left( \frac{U}{I} \right) = \frac{\Delta\gamma}{2} \sin 2\psi - \Delta\delta \frac{V}{I} \cos 2\psi - \frac{\Delta\gamma}{2} \left( \frac{Q}{I} \right) \left[ \frac{U}{I} \cos 2\psi + \frac{U}{I} \sin 2\psi \right], \quad (\text{D6})$$

$$\frac{d}{dz} \left( \frac{V}{I} \right) = \Delta\delta \left[ \frac{U}{I} \cos 2\psi - \frac{Q}{I} \sin 2\psi \right] - \frac{\Delta\delta}{2} \left( \frac{V}{I} \right) \left[ \frac{Q}{I} \cos 2\psi + \frac{U}{I} \sin 2\psi \right], \quad (\text{D7})$$

where  $\Delta\gamma = \gamma_x - \gamma_y$  and  $\Delta\delta = \delta_x - \delta_y$ .

Denote  $q = Q/I$ ,  $u = U/I$  and  $v = V/I$ , the above equations become

$$\frac{d \ln I}{dz} = -\frac{\gamma_x + \gamma_y}{2} + \frac{\Delta\gamma}{2} [q \cos 2\psi + u \sin 2\psi], \quad (\text{D8})$$

$$\frac{dq}{dz} = \frac{\Delta\gamma}{2} \cos 2\psi + \Delta\delta v \sin 2\psi - \frac{\Delta\gamma}{2} q [q \cos 2\psi + u \sin 2\psi], \quad (\text{D9})$$

$$\frac{du}{dz} = \frac{\Delta\gamma}{2} \sin 2\psi - \Delta\delta v \cos 2\psi - \frac{\Delta\gamma}{2} u [q \cos 2\psi + u \sin 2\psi], \quad (\text{D10})$$

$$\frac{dv}{dz} = \Delta\delta [u \cos 2\psi - q \sin 2\psi] - \frac{\Delta\gamma}{2} v [q \cos 2\psi + u \sin 2\psi], \quad (\text{D11})$$

The polarization is then equal to

$$p = \sqrt{q^2 + u^2}. \quad (\text{D12})$$

### D2 Linear Polarized Light

Since we are interested in the polarization by dichroic extinction from near UV to near infrared wavelength, we can disregard the emission term (second term in Equation of I) in radiative transfer (RT) equations. Moreover, by disregarding the second order terms of  $q$  and  $u$ , we obtain

$$\frac{d \ln I}{dz} = -\frac{\gamma_x + \gamma_y}{2}, \quad (\text{D13})$$

$$\frac{dq}{dz} = \frac{\Delta\gamma}{2} \cos 2\psi, \quad (\text{D14})$$

$$\frac{du}{dz} = \frac{\Delta\gamma}{2} \sin 2\psi, \quad (\text{D15})$$

Solving these equations, we obtain the Stokes parameters  $q$  and  $u$ . The polarization is simply given by [D12](#).

For the simplified case in which the magnetic field uniform and does not change along the sightline, the polarization becomes

$$p \equiv \sqrt{q^2 + u^2} = \int (dp/dz) dz, \quad (\text{D16})$$

where

$$\frac{dp}{dz} = \frac{\Delta\gamma}{2} = \frac{\gamma_x - \gamma_y}{2}. \quad (\text{D17})$$

Using Equations (D3), the above equation can be rewritten as

$$dp = \int_{a_{\min}}^{a_{\max}} \left( \frac{C_x - C_y}{2} \right) \frac{dn}{da} da dz = \int_{a_{\text{ali}}}^{a_{\max}} \left( \frac{C_x - C_y}{2} \right) \frac{dn}{da} da dz \quad (\text{D4})$$

where the assumption that grains smaller than  $a_{\text{ali}}$  are randomly oriented such that  $C_x - C_y = 0$ . For  $a > a_{\text{ali}}$ , the polarization cross-section  $C_x - C_y$  is given in Equation (C10).

#### APPENDIX E: RELATION BETWEEN $A_V$ AND $\tau_V^{\text{CAS}}$

For a spherical cloud of radius  $r_c$ , the distance from the grain located at  $(x, z)$  to the  $\gamma$  Cas is described by

$$\Delta x_s = r_c - \sqrt{r_c^2 - z^2}. \quad (\text{E1})$$

When the gas density is uniform, the optical depth relative to  $\gamma$  Cas is obtained from the visual extinction to the background star as follows:

$$1.086 \tau_V^{\text{Cas}} \equiv A_V^{\text{max}} / 2 - [(A_V^{\text{max}} / 2)^2 - (A_V / 2)^2]^{1/2}, \quad (\text{E2})$$

where  $A_V^{\text{max}}$  is the visual extinction for the line of sight going through the IC 63 center.

#### REFERENCES

- Alves F. O., Frau P., Girart J. M., Franco G. A. P., Santos F. P., Wiesemeyer H., 2014, *Astronomy and Astrophysics*, 569, L1
- Andersson B.-G., Lazarian A., Vaillancourt J., 2015, *AR&AA*
- Andersson B.-G. et al., 2013, *ApJ*, 775, 84
- Andersson B.-G., Pintado O., Potter S. B., Straižys V., Charcos-Llorens M., 2011, *A&A*, 534, 19
- Andersson B.-G., Potter S. B., 2007, *ApJ*, 665, 369
- Andersson B.-G., Potter S. B., 2010, *ApJ*, 720, 1045
- Barnett S. J., 1915, *Physical Review*, 6, 239
- Bethell T. J., Chepurnov A., Lazarian A., Kim J., 2007, *ApJ*, 663, 1055
- Cazaux S., Tielens A. G. G. M., 2004, *ApJ*, 604, 222
- Chandrasekhar S., Fermi E., 1953, *ApJ*, 118, 113
- Chiar J. E. et al., 2006, *ApJ*, 651, 268
- Cho J., Lazarian A., 2005, *ApJ*, 631, 361
- Cuppen H. M., Herbst E., 2005, *MNRAS*, 361, 565
- Davis L. J., Greenstein J. L., 1951, *ApJ*, 114, 206
- Dolginov A. Z., Mitrofanov I. G., 1976, *Ap&SS*, 43, 291
- Draine B. T., 2003, *ApJ*, 598, 1026
- Draine B. T., Lazarian A., 1998, *ApJ*, 508, 157
- Draine B. T., Weingartner J. C., 1996, *ApJ*, 470, 551
- Draine B. T., Weingartner J. C., 1997, *ApJ*, 480, 633
- Dunkley J. et al., 2009, in *CMB POLARIZATION WORKSHOP: THEORY AND FOREGROUNDS: CMBPol Mission Concept Study*. AIP Conference Proceedings. pp 222–264
- Fleming B., France K., Lupu R. E., McCandliss S. R., 2010, *ApJ*, 725, 159
- France K., Andersson B.-G., McCandliss S. R., Feldman P. D., 2005, *ApJ*, 628, 750
- Hall J. S., 1949, *Science*, 109, 166
- Hildebrand R. H., 1988, *Royal Astronomical Society*, 29, 327
- Hiltner W. A., 1949, *Nature*, 163, 283
- Hoang T., Draine B. T., Lazarian A., 2010, *ApJ*, 715, 1462
- Hoang T., Lazarian A., 2008, *MNRAS*, 388, 117
- Hoang T., Lazarian A., 2009a, *ApJ*, 697, 1316
- Hoang T., Lazarian A., 2009b, *ApJ*, 695, 1457
- Hoang T., Lazarian A., 2014, *MNRAS*, 438, 680
- Hoang T., Lazarian A., Martin P. G., 2013, *ApJ*, 779, 152
- Hoang T., Lazarian A., Martin P. G., 2014, *ApJ*, 790, 6
- Jansen D. J., van Dishoeck E. F., Black J. H., 1994, *Astronomy and Astrophysics* (ISSN 0004-6361), 282, 605
- Jansen D. J., van Dishoeck E. F., Black J. H., Spaans M., Sosin C., 1995, *A&A*, 302, 223
- Jansen D. J., van Dishoeck E. F., Keene J., Boreiko R. T., Betz A. L., 1996, *A&A*, 309, 899
- Jones R. V., Spitzer L., 1967, *ApJ*, 147, 943
- Jones T. J., Bagley M., Krejny M., Anderson B.-G., Bastien P., 2014, *arXiv.org*
- Jones T. J., Klebe D., Dickey J. M., 1992, *ApJ*, 389, 602
- Katz N., Furman I., Biham O., Pirronello V., Vidali G., 1999, *ApJ*, 522, 305
- Lazarian A., 1995, *MNRAS*, 274, 679
- Lazarian A., 1997, *MNRAS*, 288, 609
- Lazarian A., 2007, *J. Quant. Spectrosc. Rad. Trans.*, 106, 225
- Lazarian A., Draine B. T., 1997, *ApJ*, 487, 248
- Lazarian A., Draine B. T., 1999, *ApJ*, 516, L37
- Lazarian A., Hoang T., 2007a, *MNRAS*, 378, 910
- Lazarian A., Hoang T., 2007b, *ApJ*, 669, L77
- Lazarian A., Hoang T., 2008, *ApJ*, 676, L25
- Lazarian A., Roberge W. G., 1997, *ApJ*, 484, 230
- Mathis J. S., Mezger P. G., Panagia N., 1983, *A&A*, 128, 212
- Matsumura M., Kameura Y., Kawabata K. S., Akitaya H., Isogai M., Seki M., 2011, *Publications of the Astronomical Society of Japan*, 63, L43
- Mezger P. G., Mathis J. S., Panagia N., 1982, *A&A*, 105, 372
- Pelkonen V.-M., Juvela M., Padoan P., 2009, *A&A*, 502, 833
- Pirronello V., Biham O., Liu C., Shen L., Vidali G., 1997, *ApJL*, 483, L131
- Pirronello V., Liu C., Roser J. E., Vidali G., 1999, *A&A*, 344, 681
- Planck Collaboration et al., 2014a, *arXiv:1409.5738*, p. 5738
- Planck Collaboration et al., 2014b, *arxiv:1405.0871*, p. 871
- Polehampton E. T., Wyrowski F., Schilke P., Güsten R., 2005, in *IAU Symposium*. p. 148P
- Purcell E. M., 1979, *ApJ*, 231, 404
- Purcell E. M., Spitzer L., 1971, *ApJ*, 167, 31
- Rachford B. L. et al., 2009, *ApJ*, 180, 125
- Roberge W. G., Degraff T. A., Flaherty J. E., 1993, *ApJ*, 418, 287
- Roberge W. G., Lazarian A., 1999, *MNRAS*, 305, 615
- Spitzer L., McGlynn T. A., 1979, *ApJ*, 231, 417
- Sun X. H., Han J. L., Reich W., Reich P., Shi W. B., Wielebinski R., Fürst E., 2007, *A&A*, 463, 993
- Weingartner J. C., 2009, *ApJ*, 690, 875
- Weingartner J. C., Draine B. T., 2001, *ApJ*, 548, 296
- Whittet D. C. B., Hough J. H., Lazarian A., Hoang T., 2008, *ApJ*, 674, 304
- Xu Y. et al., 2013, *ApJ*, 769, 15